Faults modulate magma propagation and triggered seismicity: the 2022 São Jorge (Azores) volcanic unrest

Stephen P. Hicks[1,✢], Pablo J. Gonzalez[2,✢], Anthony Lomax[3], Ana M.G. Ferreira[1], Ricardo S. Ramalho[4], Neil C. Mitchell[5], Graça Silveira[6,7], Nuno Afonso Dias[6,7], João Fontiela[8], Rui Fernandes[9], Susana Custódio[6], Maria Tsekhmistrenko[1], Virgilio Mendes[6], Adriano Pimentel[10,11], Rita Silva[10,11], Gonçalo Prates[12,13], William Sturgeon[1], Augustin Marignier[1], Fernando Carrilho[14], Rui Marques[10,11], Miguel Miranda[6,15], Arturo M. Garcia[10,11].

1. Department of Earth Science, University College London, London, United Kingdom.
2. Volcanology Research Group, Department of Life and Earth Sciences, Instituto de Productos Naturales y Agrobiología, Consejo Superior de Investigaciones Científicas (IPNA-CSIC), La Laguna, Spain.
3. ALomax Scientific, Mouans Sartoux, France.
4. School of Earth and Environmental Sciences, Cardiff University, Cardiff, United Kingdom.
5. Department of Earth and Environmental Sciences, University of Manchester, Manchester, United Kingdom.
6. Instituto Dom Luiz, Faculdade de Ciências, Universidade de Lisboa, Lisbon, Portugal.
7. Instituto Superior de Engenharia de Lisboa, Instituto Politécnico de Lisboa, Lisbon, Portugal
8. Institute of Earth Sciences, University of Évora, Portugal.
9. Instituto Dom Luiz, University of Beira Interior, Covilhã, Portugal.
10. Instituto de Investigação em Vulcanologia e Avaliação de Riscos (IVAR), Universidade dos Açores, Azores, Portugal.
11. Centro de Informação e Vigilância Sismovulcânica dos Açores (CIVISA), Azores, Portugal.
12. Instituto Superior de Engenharia, University of Algarve, Faro, Portugal.
13. Centro de Estudos Geográficos, IGOT, University of Lisbon, Lisbon, Portugal.
14. Divisão de Geofísica, Instituto Português do Mar e da Atmosfera, Lisbon, Portugal.
15. AIR Centre, Azores, Portugal

✢ Equally-contributing authors

Abstract

Understanding the signatures and mechanisms of failed volcanic eruptions is vital for mapping magma plumbing systems and forecasting volcanic events. Geological structures, such as faults and fractures, play a crucial role in guiding magma, but their mechanisms remain unclear due to the lack of 3-D mapping of faults in volcanic regions and sufficiently precise earthquake locations. The triple-junction setting of the Azores Archipelago, where volcanic systems and seismogenic crustal faults coexist, provides a unique insight into the interaction between faults and magma. Using ~18,000 earthquakes relocated to ultra-high precision with onshore and ocean-bottom seismometer data, along with geodetic observations and seismic autocorrelation imaging, we analyse a failed eruption in 2022 on São Jorge Island. A magmatic dike, likely originating in the upper mantle, ascended rapidly, largely aseismically, and without apparent precursory surface deformation, into a crustal fault, before stalling beneath the island edifice, 1,600 m below the surface. Adjacent seismicity suggests that the ascending magma stalled, probably due to minor melt branching and fluids escaping laterally along the fault zone, triggering an intense, months-long seismic swarm, comprising rotated focal mechanisms. Our study reveals the dual role of fault zones in both facilitating and arresting magma ascent, highlighting the interplay between tectonism and magmatism.

1. Introduction

Magma that ascends to the Earth's surface causes volcanic eruptions, but it can also stall at various depths, including the shallow crust, leading to *failed* eruptions[1]. Understanding the mechanisms of magmatic ascent is key to interpreting volcanic unrest and the formation of the crust. The final fate of magma depends on several factors, like its pressure relative to the crustal rock stress state[2], fracture toughness at the dike tip[3], and internal magma dynamics (e.g., density, resupply of magma, degassing/devolatilisation[4], crystallisation[1]).

Pre-existing faults and fractures play a crucial but underexplored role in magma dynamics. Faults can capture and guide melt[5], providing energetically favourable pathways[6–8] for it to reach the surface[7,9]. Alternatively, magma may stall due to fluid circulation[10], or if the fault is misoriented for opening[9,11]. While fault architecture is proven to influence fluid flow and seismogenesis[12], the mechanical link between faults and magmatism remains less well understood[13–15]. Spatio-temporal patterns of volcano-tectonic (VT) seismicity can reveal magma pathways[16,17]. However, a key challenge in disentangling the role of faults and fractures proximal to magma movement is obtaining sufficiently accurate and precise earthquake locations relative to fault length-scales[18], a particularly challenging

task in ocean island settings, where island and inter-island geography limit seismometer network coverage and geodetic observations.

In contrast to classical orthogonal rifts (e.g., Afar, East Africa), transtensional environments provide insight into the interaction between pre-existing faulting structures and magmatism, and how they accommodate plate motion. In SW Iceland, dikes strike perpendicular to tectonic extension[7], triggering seismicity along oblique faults that accommodate the strike-slip component of plate motion[19]. However, such cases still somewhat conceal the more direct role of faults in magma ascent, leaving a knowledge gap in how larger, proximal faults influence magma movement[20] and feedback mechanisms between tectonics, magmatism and seismogenesis.

Unlike Iceland, the coexistence of active magmatic systems and seismogenic crustal-scale faults in the Azores hotspot and triple-junction region offers a clearer view of the interplay between tectonic structures and magmatism[21] (Fig. 1a). The Azores is shaped by the diffuse boundary between the Eurasian and Nubian plates, with the Terceira Rift (Fig. 1a) as the main spreading system, where slow (~4.5 mm/yr), WSW-ENE-oriented relative motion[22–25], produces right-lateral transtension[26]. Past earthquakes[27–29] show rift-parallel normal faulting and off-rift strike-slip faulting (Fig. 1a). Deformation across the Azores is highly distributed, with fissure systems, off-rift transforms, grabens, and extension-oblique volcanic ridges[21,22,26,30–36], such as that expressed by São Jorge Island, located ~40 km SW of the Terceira rift axis (Fig. 1b).

São Jorge is a narrow island 55 km long and up to just 7 km wide (Fig. 1b-c). Erupted basalts show signs of a weak mantle plume[37], and fissure eruptions along a well-defined scoria cones have generally migrated 5 cm/yr westwards over 750 kyr[22]. These volcanic alignments lie along strike-slip fault zones, reflecting magmatic-tectonic interplay[22,24]. In the west of São Jorge, two major fault zones (Fig. 1c, Fig. 2), Picos (P-FZ; striking WNW–ESE) and Pico do Carvão (PdC-FZ; striking almost E-W) feature scoria/spatter cones and craters[35]. The PdC-FZ hosted eruptions in 1580, 1808, and a possible submarine eruption in 1964[38,39]. Historically, the island hosted one of the largest earthquakes in the Azores, estimated at *M* 7.5, in 1757[40–43]. Paleoseismology shows that the right-laterally offset PdC-FZ (Fig. 2) is currently the fastest-slipping fault (2.6-3.4 cm/yr) on São Jorge[44] and can generate *M*~7 earthquakes[35,44].

Starting on 19 March 2022, São Jorge experienced a highly active seismic swarm[45], with microseismicity continuing for at least two years. Our ultra-high-precision hypocentre locations from onshore and offshore seismic data, reconciled with modelling of surface deformation observations, reveal a crustal fault that plays a dual role as both a pathway and a barrier to magma ascent.

2. Results

2.1. Geodetic observations and dike-opening model

Daily GNSS solutions from nine stations in the Azores (Fig. 1b; see *Methods*) reveal intense deformation beginning on 19 March 2022, when the seismic swarm commenced (Figs. 3a, S1). Stations on Pico (PIED; AZTP) and Graciosa (AZGR; ENAO) moved horizontally away from São Jorge by up to 18 mm (Fig. 1b). Faial (HORT) and Terceira (PAGU; TERC) show negligible motion. Stations on São Jorge (QEMD, VLAZ) moved roughly eastward by up to 10 mm. QEMD also subsided by 5 mm. Some stations exhibit rapid deformation over just one day, while others display a slightly slower, three-day-long deformation transient (Fig. S1). Aside from long-term interplate strain accumulation, no substantial deformation occurred before or after the onset of seismicity on 2022-03-19 (Figs. 3a, S1 & S2).

Similarly, analysis of processed Sentinel-1A interferograms (see *Methods*) reveals no significant deformation signals before or after the onset of seismicity (Figs. S3-S5). During 15-21 March 2022, independent interferograms spanning 2022-02-13 to 2022-03-21 (ascending) and 2022-03-15 to 2022-03-27 (descending) detected up to +6 cm line-of-sight deformation on central São Jorge (Figs. 1c, S4 & S6). Both ascending and descending passes show a similar uplift pattern, symmetrical across the island's flanks, with lobes of maximum uplift at the coastlines ('*L1*' and '*L2*' in Fig. 1c) and negligible deformation along an 8-10 km saddle sub-parallel to the island's axis. All deformation detected by InSAR occurred between 15 and 21 March 2022 (Figs. S3-S5), consistent with the GNSS signals and the onset of seismicity.

InSAR fringe patterns and GNSS displacements north and south of São Jorge (Fig. 1b-c) indicate substantial opening, and thus a zone of tensile opening striking slightly oblique to the island's long axis. Joint inversion of three-component GNSS and both InSAR tracks with a Bayesian 3D Mixed Boundary Element Method (BEM) inversion (see *Methods*) yields a quadrangular dike-opening solution. This model is illustrated in Fig. 4, with uncertainties in the model parameters presented in Table S1 and Figs. S7-9, and which are illustrated by the fuzzy pink shading in Fig. 4b-d, based on an ensemble of 1,000 acceptable solutions. The modelled dike comprises a ~6 km-long by ~25 km deep, WNW-ESE (285° strike), near-vertical (83° ± 7° dip) body beneath the western-central island, just east of the seismicity (Fig. 4). The dike has a total volume of 79×10^6 m^3 with a maximum opening of 72 cm. The top of the dike is located ~1.65 ± 0.60 km below the surface, as required by both ascending and descending InSAR tracks, and the near-field GNSS displacements on São Jorge (QEMD, VLAZ). The inversion yields a bottom depth of the dike at ~26 km below sea level (bsl), within the lithospheric mantle[46,47]. The vertically extensive nature of the modelled dike is required by the far-field GNSS stations on adjacent islands; however, the bottom depth is one of the most uncertain aspects of the

model (formal uncertainty of ± 8 km; Figs. S7-S9; Table S1), with the best-fit model at the deeper end of the ensemble solutions, but most models reaching beyond 20 km depth bsl (Fig. 4b). The quadrangular model's top-length (4,300 ± 2,500 m) and its shear angle (-11° ± 11°; i.e., slants to the west) are reasonably well constrained, although the uncertainties in these parameters translate to a substantial variation in its along-strike areal extent (fuzzy pink shading in Fig. 4d). Although far-field GNSS vertical time series are noisy, our model predicts well the observed vertical and horizontal GNSS displacements on São Jorge and adjacent islands F(ig. S10), as well as both ascending and descending interferograms (Fig. S11).

To test the robustness of the quadrangle geometry parameterisation, we conducted an extensive exploration of the model space. These tests included evaluating a wide range of source geometries, such as single and multiple vertical, inclined, and curved dikes, spherical and ellipsoidal pressure sources, faults with both right- and left-lateral shear, and combinations of the above (Text S1). Though physically plausible, none of these alternative configurations improved fits to both GNSS and InSAR data (Table S2). Our sub-vertical quadrangular dike model emerged as the preferred solution because it is the only configuration that reconciles all datasets with small residuals and physically plausible parameters.

Previous analysis of GNSS signals[45] suggests a 2-day-long, up to 4 cm, precursory uplift signal at QEMD starting on 2022-03-16. However, given vertical-component noise levels and our daily solution uncertainties, we cannot confidently identify such a signal in our Precise Point Positioning (PPP) solution; nor does our independent network-based processing GNSS solution corroborate such a signal (Text S2; Fig. S2). The previously reported solutions[45] from QEMD show multiple similar-sized anomalies at other times, which were left uninterpreted. Furthermore, we observe no such signal at the nearby GNSS station VLAZ (Fig. S1). Nevertheless, we conducted forward modelling of the proposed sill source matching 4 cm uplift[45] with minor horizontal motion (Text S2). Such a magmatic source, if located at the depth of the intense seismicity, would have instead produced cm-scale signals at VLAZ. Therefore, we suggest that such rapid transient signals are likely GNSS processing artefacts; moreover, if the precursory uplift signal at QEMD were real, it is too small, uncertain, and too localised to be confidently quantified and modelled.

2.2. Seismicity distribution and its temporal evolution

Seismic data come from permanent networks densified by temporary stations installed in response to the seismic swarm (Figs. 1b & S12); (see *Methods* & Data Availability). Six temporary ocean bottom seismometers (OBS) offshore São Jorge enhance the inherently poor coverage due to the islands' geographic distribution and the narrow geometry of São Jorge (Fig. 1b). Using data from 83 stations, our automated workflow (see *Methods*) gives ultra-high precision relative relocations for 18,049

events. All events have a maximum azimuthal gap of <240°, a maximum RMS residual of 0.4 s, and a maximum semi-major axis length of 1,500 m. The median depth uncertainty of all events in the catalogue is 46 m.

Deep precursory seismicity

From June 2021 (nine months before the onset of unrest), we identified 36 events at ~30 km depth bsl south of São Jorge (Figs. 3b-d & 4).. The largest of these earthquakes has a moment magnitude (M_w) of 2.6. Our high-precision relative relocations show that these events, forming three main clusters, progressively migrated northward (labelled Deep, *D1*-3 in Figs. 3b-d & 4), starting beneath the Canal de São Jorge (São Jorge channel, south of the island), to ~2 km inland of the coastline, gradually shallowing from ~32 km to ~25 km depth (Fig. 4b). Waveform template matching[49] with these well-located events finds a greater number of events (150) that could not be accurately located (Fig. 3c), but affirm short, migrating bursts of discontinuous seismicity (Fig. 3b-d), separated by more extended aseismic periods. Based on our results, the two weeks immediately before the onset of the seismic swarm were aseismic.

First 24 hours of the seismic swarm

The seismic swarm started abruptly at ~1702 UTC on 19 March 2022, coinciding with the onset of geodetically observed deformation (Fig. 3a-b). We find many earthquake-like signals starting at least 3 hours earlier, and accelerating in rate, although they are too small to be located. During the first 9 hours, we find 120 events of which nine have M_w > 3.0, with a very high-rate of seismicity (up to 50 earthquakes per hour) persisting over the first 24 hours (Fig. 5a). We detected two phases of tremor-like bursts (see *Methods*) during this time (Fig. 5b). The first coinciding with the start of the swarm; the other ~6 hours later both marking the onset of accelerating seismicity rat,. The first locatable earthquake occurred at 9 km depth within the vicinity of the modelled dike, and subsequent seismicity appears to migrate upwards to ~5 km depth, and spread bilaterally, forming two shallow branches of rapidly-upward migrating seismicity at ~400 m/hour ("*SB*" in Figs. 4 & 5). Almost concurrently, seismicity then migrates ~8 km westward and ~3 km downward at ~400-800 m/hour to depths of 8-13 km, where the main zone of seismicity develops and remains for subsequent months.

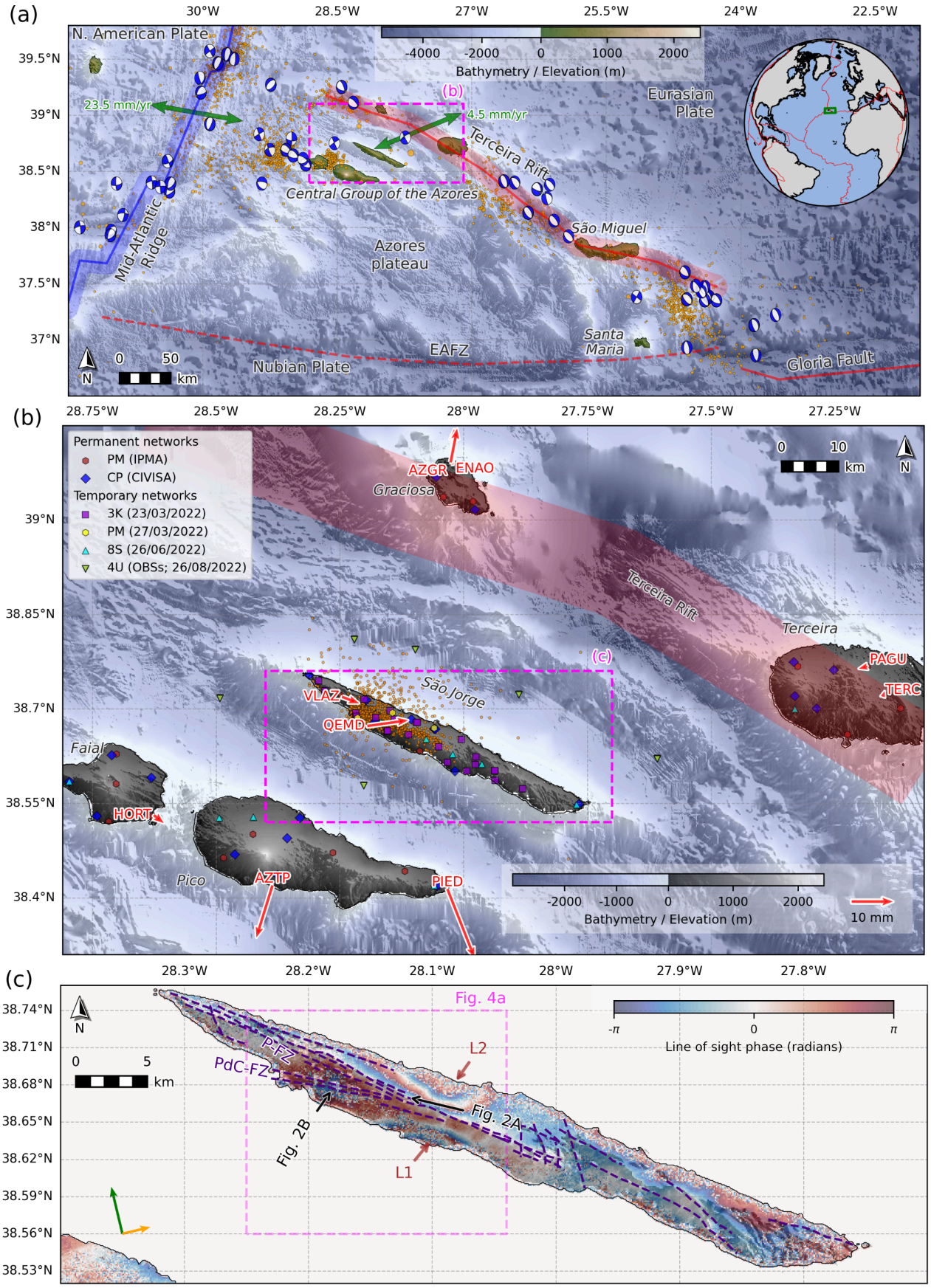
(a)
30°W
28.5°W
27°W
25.5°W
24°W
22.5°W
39.5°N
39°N
38.5°N
38°N
37.5°N
37°N
N. American Plate
-4000
-2000
0
1000
2000
Bathymetry / Elevation (m)
(b)
23.5 mm/yr
4.5 mm/yr
Eurasian Plate
Terceira Rift
Central Group of the Azores
São Miguel
Azores plateau
Mid-Atlantic Ridge
Santa Maria
EAFZ
Nubian Plate
Gloria Fault
N
0
50
km
(b)
28.75°W
28.5°W
28.25°W
28°W
27.75°W
27.5°W
27.25°W
39°N
38.85°N
38.7°N
38.55°N
38.4°N
Permanent networks
PM (IPMA)
CP (CIVISA)
Temporary networks
3K (23/03/2022)
PM (27/03/2022)
8S (26/06/2022)
4U (OBSs; 26/08/2022)
AZGR
ENAO
Graciosa
0
10
km
N
Terceira Rift
Terceira
PAGU
TERC
(c)
São Jorge
VLAZ
QEMD
Faial
HORT
Pico
AZTP
PIED
-2000
-1000
0
1000
2000
Bathymetry / Elevation (m)
10 mm
(c)
28.3°W
28.2°W
28.1°W
28°W
27.9°W
27.8°W
38.74°N
38.71°N
38.68°N
38.65°N
38.62°N
38.59°N
38.56°N
38.53°N
N
0
5
km
Fig. 4a
-π
0
π
Line of sight phase (radians)
P-FZ
PdC-FZ
L2
Fig. 2A
Fig. 2B
L1

Fig. 1: Seismotectonic context, stations, and surface deformation. *a) Tectonic configuration of the Azores region, showing pre-2022 M>3.5 background seismicity (orange circles)[48]. Double-couple components are plotted for moment tensors[28]. Green arrows show relative plate motions[23]. EAFZ = East Azores Fracture Zone. b) Map of the Central Group islands of the Azores showing locations of permanent and temporary seismic stations. Red arrows show horizontal GNSS solution displacement vectors from 17/03/2022 - 22/03/2022, with station names labelled in red. Orange circles show the routine seismic locations of the 2022 seismic swarm from CIVISA. c) Wrapped ascending interferogram from the Sentinel-1A satellite spanning 2022/02/13 - 2022/03/21. Fig. S6 shows the unwrapped interferogram. Green and orange arrows indicate the satellite azimuth and look direction, respectively. The brown annotations show the two lobes of uplift in the interferogram. Dark blue dashed lines indicate mapped faults and volcanic alignments on São Jorge[35,44]. Black arrows show the aerial imagery in Fig. 2.*

Main zone of seismicity

Subsequent westward and downward migration formed the main zone of seismicity at 8-13 km depth, residing near the estimated crust-mantle transition beneath São Jorge based on our inverted 1-D velocity model (Fig. 5) and independent estimates of Moho depth[47]. These epicentres, including the earlier shallow branches of seismicity (*SB*), form a narrow (<500 m width), WNW-ESE lineation along the mapped surface trace of the PdC-FZ (Fig. 4a), slightly oblique to the island's long axis. Along a profile perpendicular to the PdC-FZ (Fig. 4b-c), events at 8-12 km form a near-vertical, NNE-dipping structure directly west of the modelled dike, comprising distinct sub-streaks. On a PdC-FZ-parallel cross-section (Fig. 4d), most events align along two gentle (~10°) west-dipping lineations: one at 8-11 km depth (labelled Upper Lineation, "*UL*" in Fig. 4d) with substantial internal complexity showing many sub-vertical filaments (Fig. 6), and the other at 11-12 km with sub-horizontal streaks (Lower Lineation, "*LL*" in Fig. 5d). These are separated by a ~2 km-wide aseismic region ("*AS*" in Fig. 5d). Additional seismic clusters and streaks occur even deeper, at 12-14 km ("*DL*"). Based on clustering of waveform pair cross-correlations[50], we find 22 distinct clusters comprising at least 50 events (Fig. 6a). Clusters in UL appear to show a slow upward migration with time (Movie S1), whose front is consistent with a fluid diffusivity of ~0.001-0.002 m^2/s (Fig. 6b-c).

Following the early intense period of high-rate seismicity and tremor, the remaining seismicity appears as high-frequency signals with impulsive onsets (Fig. 6d), typical of VT events. After the first nine hours of the swarm, we found no additional tremor-like signals. The seismic swarm overall has a remarkably high *b*-value of 2.4 ± 0.1 (Fig. S13) based on M_w estimates from spectral inversion (see *Methods*; Figs. S14-15). Well-constrained focal mechanisms (see *Methods*; Fig. S16) show strike-slip faulting, with one nodal plane parallel to the main lineation of seismicity and the PdC-FZ, indicating left-lateral faulting (Fig. 4a). Dense coverage of *P*-wave polarities across the focal sphere for ~40 earthquakes indicates double-couple failure (Fig. S16).

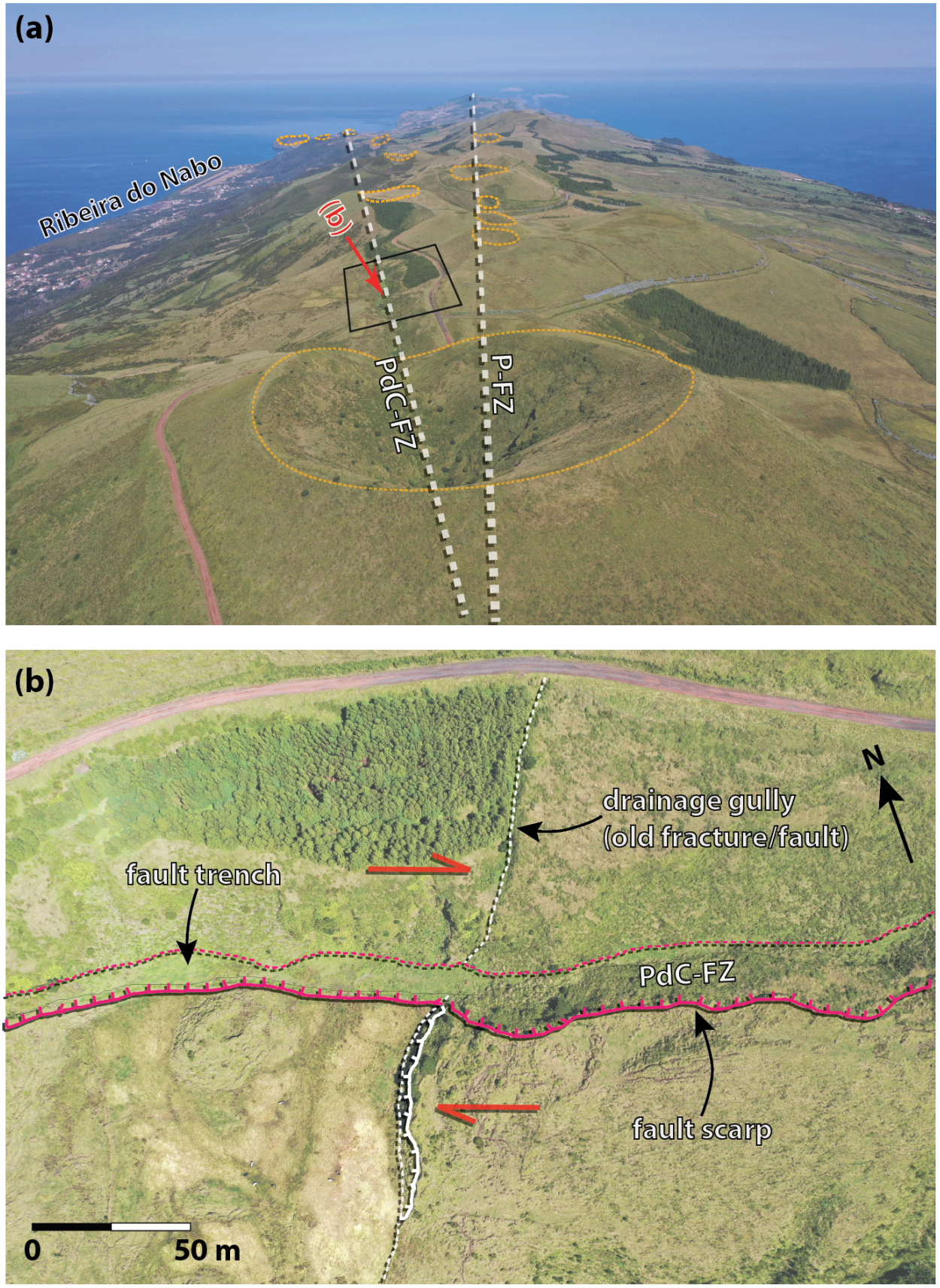

Fig. 2: Drone imagery showing surface faulting on São Jorge near the 2022 unrest area. *P-FZ = Picos fault zone; PdC-FZ = Pico do Carvão fault zone. (a) View looking west-north-west (see Fig. 1c for camera position and direction). Dotted orange lines highlight the vents of fissure eruptions. (b) Evidence of right-lateral offsets along the PdC-FZ (see Fig. 1c and Fig. 3a for location).*

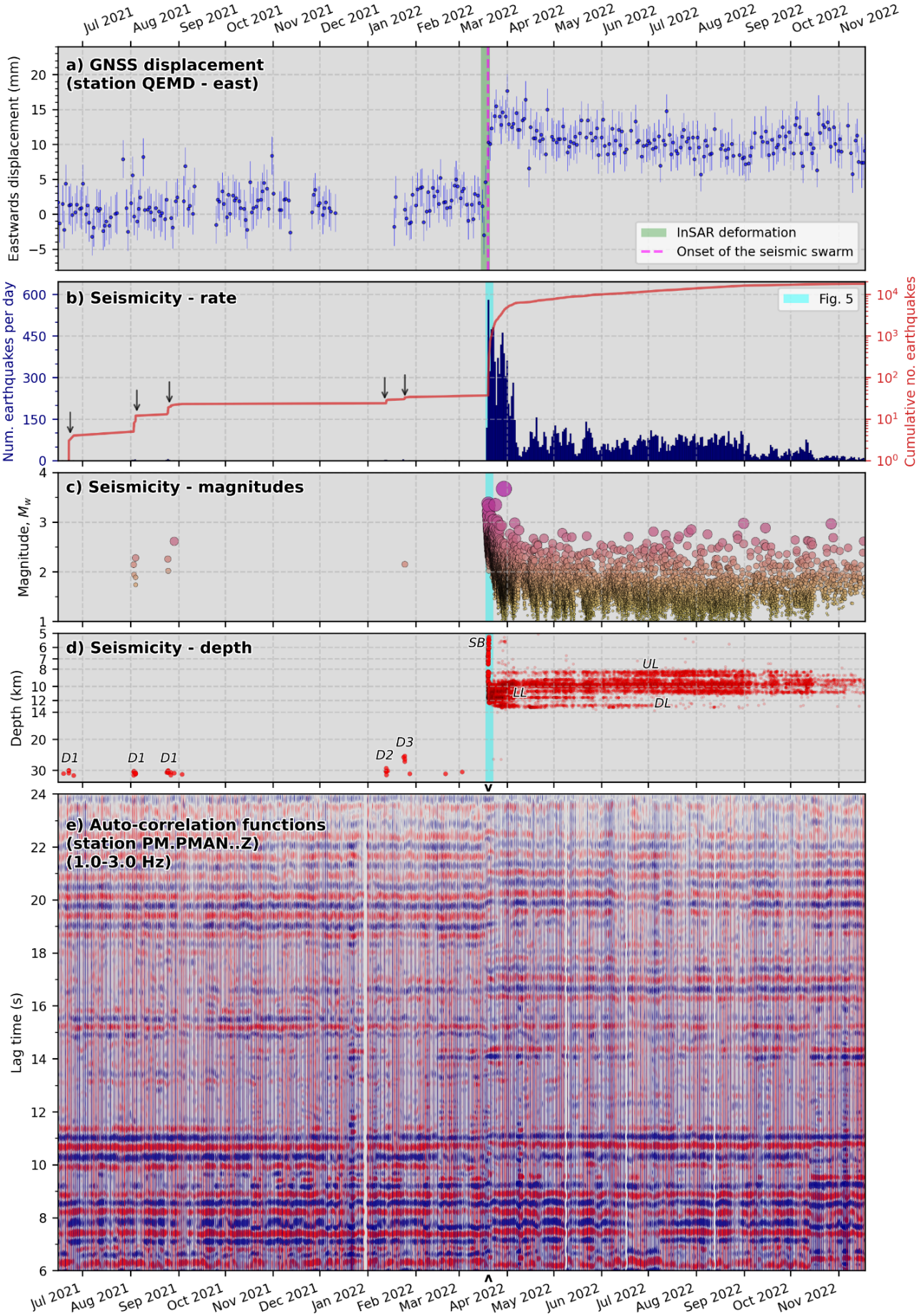
a) GNSS displacement
(station QEMD - east)
Eastwards displacement (mm)
InSAR deformation
Onset of the seismic swarm
b) Seismicity - rate
Num. earthquakes per day
Cumulative no. earthquakes
Fig. 5
c) Seismicity - magnitudes
Magnitude, M_w
d) Seismicity - depth
Depth (km)
SB
UL
LL
DL
D1
D2
D3
e) Auto-correlation functions
(station PM.PMAN..Z)
(1.0-3.0 Hz)
Lag time (s)
Jul 2021
Aug 2021
Sep 2021
Oct 2021
Nov 2021
Dec 2021
Jan 2022
Feb 2022
Mar 2022
Apr 2022
May 2022
Jun 2022
Jul 2022
Aug 2022
Sep 2022
Oct 2022
Nov 2022

Fig. 3: Evolution of the 2022 São Jorge unrest and precursory seismicity. *a) Processed daily eastwards GNSS displacements at station QEMD (location shown in Fig. 1b) with error bars, and the inferred period of InSAR detectable deformation labelled (Figs. 1c, S3-S5). Displacements are given within a global reference frame, with the secular trend removed. Time series for other GNSS stations are shown in Fig. S1. Panels (b), (c), and (d) show the time evolution of seismicity rate, moment magnitude, and depth, respectively. The blue vertical stripe denotes the time window shown in Fig. 5. Downward-pointing black arrows in (b) denote bursts of precursory deep seismicity. In (c), circle sizes are scaled by magnitude. Note the logarithmic depth axis in (d). Labels denote the main seismicity clusters shown in Figs. 4-6 and described in the main text. = e) Autocorrelation results from the vertical component of station PM.PMAN (location shown in Fig. 4) show changes in subsurface properties at the onset of the seismic swarm. Red and blue colours represent positive and negative amplitudes, respectively, in the ACF waveforms. At the onset of the seismic-volcanic unrest (indicated by the small black arrowheads above and below the time axis), the ACFs at lag times of <8 s and >18 s become less coherent and shifted in time.*

2.3. Subsurface velocity changes

To assess possible subsurface structural changes before, during, and after the seismic swarm, we analysed ambient noise phase autocorrelation functions[51] (ACFs) from 1-3 Hz filtered vertical-component waveform data to yield subsurface *P*-wave reflection responses (see *Methods*). Given that only three permanent stations on São Jorge captured the onset of the unrest, we retrieved high-quality and stable ACF results from PM.PMAN and PM.ROSA (station locations shown in Figs. 4a & d. Pre-unrest reference ACFs from May to September 2021 show coherent arrivals at lag times of ~6-24 s (Figs. 3e & S17). When the seismic swarm and surface deformation began on 19 March 2022, PM.PMAN's ACFs showed a sharper shift to higher lags, especially in the 8-11 s and 18-24 s ranges (Fig. 3e), indicating velocity reductions at <10 km and >15 km depth, respectively, based on our 1-D velocity model (Figs. 4b & S18). Stronger reflections also appear at 16-18 s on 2022-03-19. In contrast, PM.ROSA's ACF shows less stable and less systematic variations at the onset of unrest (Fig. S17). These two stations are ~16 km apart, and given the waveform frequency and inferred depth of subsurface changes, we infer that PM.PMAN sensitivity kernel includes the geodetically imaged main dike, whereas PM.ROSA is too far west of the dike (Fig. 4).

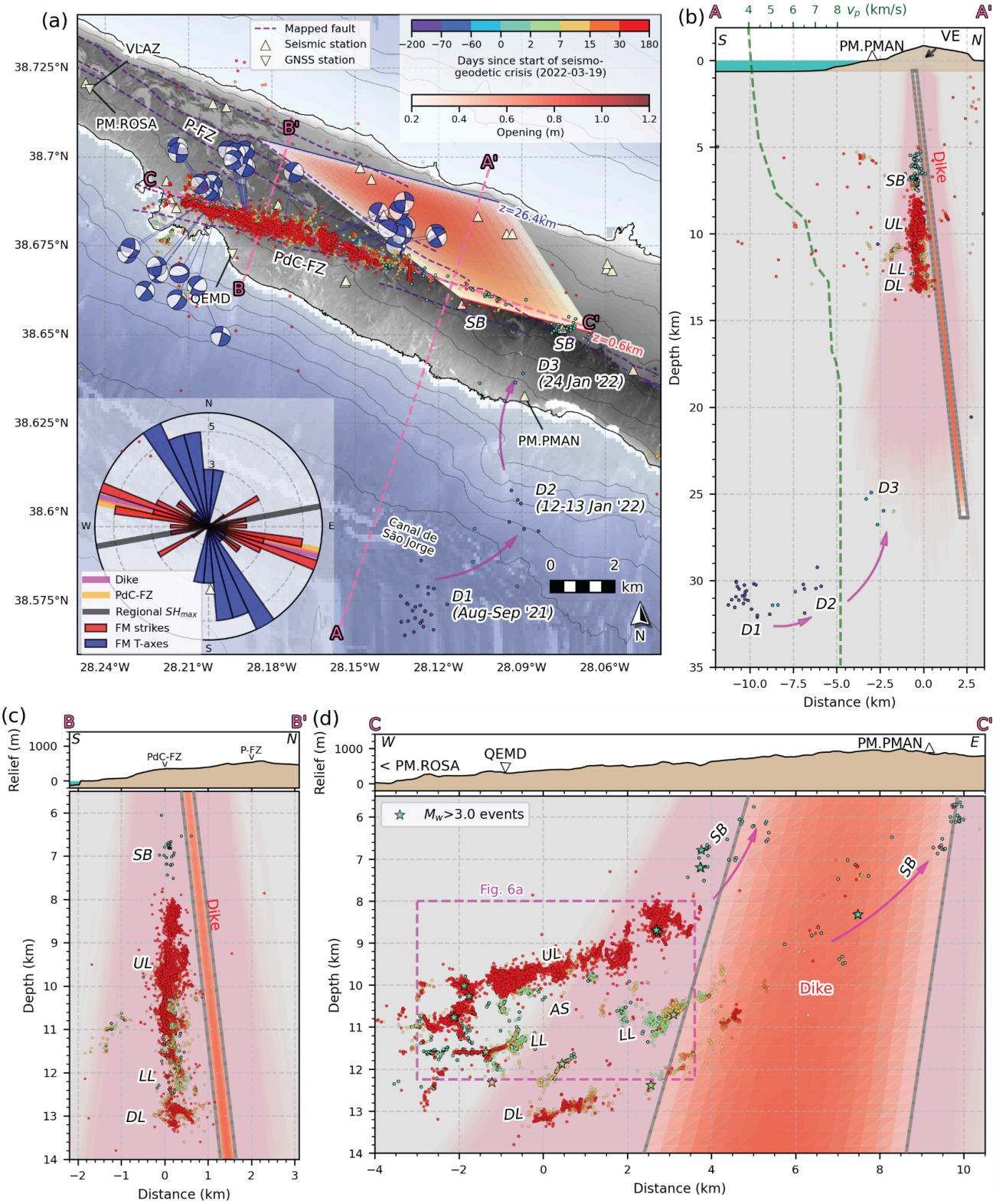

Fig. 4: High-precision seismicity relocations and joint GNSS-InSAR dike opening model. *(a) Map view, with seismic events coloured according to their depth. Purple dashed lines are surface fault traces and volcanic alignments[24,44]. Magenta arrows show the migration of precursory and early seismicity. White triangles are seismic stations. Contour lines are plotted for every 250 m of elevation. The inset rose diagram shows focal mechanism strikes compared with the dike and mean strike of mapped faults, along with a comparison between the inferred regional SHmax direction (Fig. 1a) and focal-mechanism T-axes. (b) Seismicity-perpendicular cross-section, A-A'. IE = island edifice. The dashed green line shows the P-wave velocity from our 1-D model (Fig. S6). c) Seismicity-parallel cross-section, with a focus on the main clusters of seismicity. d) Along-strike cross-section, C-C'. Labelled clusters of seismicity are discussed in the text. Note the break in range of the vertical axes between the relief and seismicity cross sections in (c) and (d). In all cross-sections, the fuzzy pink shading illustrates model uncertainty, based on an ensemble of the 1000 lowest-misfit geodetic diking solutions. These models represent the range of plausible dike geometries consistent with the observed deformation (InSAR and GNSS).*

3. Discussion

Using our high-precision seismicity catalogue, focal mechanisms, geodetic model, and seismic autocorrelation function imaging, we have developed a model for the 2022 São Jorge seismic-volcanic unrest, illustrated in Fig. 7, and detailed below.

Our geodetic dike opening model indicates magma intrusion from 1 to 26 km bsl (Fig. 4), with no significant inflation preceding it (Figs. S1 & S2). The precursory earthquakes in the upper mantle (25–35 km depth) correlate well with the modelled dike's base (Fig. 4). Even though our best-fitting model dips slightly to the north, many acceptable models in the ensemble have slight southerly dips (Figs. 4b, S7-S9) and even directly reach the final phase of deep seismicity that was active just ~2 months before the main seismic swarm (*D3*).[52,53]. Such deep precursory seismicity[18,54–56] is often interpreted as magma accumulation or destabilisation in migrating deep reservoirs[56–58], with a depth of 25-35 km consistent with those obtained by fluid inclusion barometry of São Jorge lavas[51,52].

Our geodetic observations and dike model imply rapid magma ascent, possibly involving near-simultaneous dike opening in the crust and upper mantle. Vertically extensive and rapid melt ascent is also supported by our ambient noise ACF results, which show rapid structural changes at PM.PMAN, the station located closest to the ascending dike (Figs. 3d & 4). The deep (> 9 km) and shallow (< 5 km) portions of melt ascent were aseismic. Only two moderately-dipping branches of seismicity (*'SB'* in Figs. 3-5), plus associated tremor, appear to be the only seismogenic response of the ascending intrusion; these initiated at ~8-9 km depth, and rapidly migrated upward to ~5.5 km depth during the first few hours of the seismic swarm. Given that both of these shallow seismicity branches became inactive within a few hours, and considering their time-space correlation with the geodetic dike model, along with its inherent uncertainty, these shallow earthquakes and tremor-like bursts likely mark the flanks of the ascending dike.

Our geodetic model shows that magma stalled ~1,600 m below the surface, near the estimated base of the island edifice, based on surrounding bathymetry (Fig. 4). We are not aware of any monitoring infrastructure, data, or reports (peer-reviewed or otherwise) of gas geochemical anomalies observed during the dike intrusion and start of the seismic swarm. The short-lived nature of the intrusion and the different permeability conditions of the volcanic island edifice may have inhibited efficient gas escape to the surface. Magma propagation is governed by a combination of fracture toughness, overpressure, buoyancy, and viscosity[3], so an explanation for stalling at this depth is that the volume of magma, and hence the resulting overpressure, may have been insufficient to overcome the lithostatic and edifice-related stresses at shallow depths. A dynamic increase in magma viscosity, such as due to devolatilisation[4], may have also inhibited magma ascent. These factors, acting

individually or in combination, likely led to the observed stalling of the dike at the base of the island edifice.

The dike intruded parallel to the PdC-FZ and VT seismicity zone, east of the surface-mapped fault zone, where the fault is likely buried by lavas and scoria cones (Fig. 4). The fault therefore provides a direct structural and hydraulic connection between the dike and seismicity. Unlike typical dike intrusions, where seismicity surrounds the dike in a 'dogbone' pattern[16,60–67], the 2022 São Jorge seismic-volcanic unrest shows seismicity confined to one flank of the dike with no activity within or to the east of the dike. Few similarly oriented faults have been mapped on the eastern side of the island (Fig. 1c), and the long-lived segmentation of three volcanic complexes across the island[24] might have controlled the localisation of triggered seismicity. The PdC-FZ and seismicity lie in a zone positively stressed by the modelled dike intrusion, both for left- and right-lateral strike-slip failure on receiver faults (>50 kPa; Figs. S19-S20). However, similarly oriented and stressed nearby structures, like the P-FZ, remained aseismic. Such asymmetrically localised seismicity is thus likely due to the PdC-FZ providing a direct hydraulic connection between the westward-tilting intruded dike and earthquakes, allowing fluids to trigger seismicity directly. The PdC-FZ is a major mantle-rooted structure in the central Azores that accommodates regional transtension[24,38,44,53], and appears to have been the locus of recent magmatic and seismogenic activity on the island, given its recent eruptive history and capability to generate M_w~7 earthquakes[44], likely involving complete crustal rupture. Such events, along with long-term tectonics, may have pre-loaded the fault in the lead-up to the 2022 seismic-volcanic unrest.

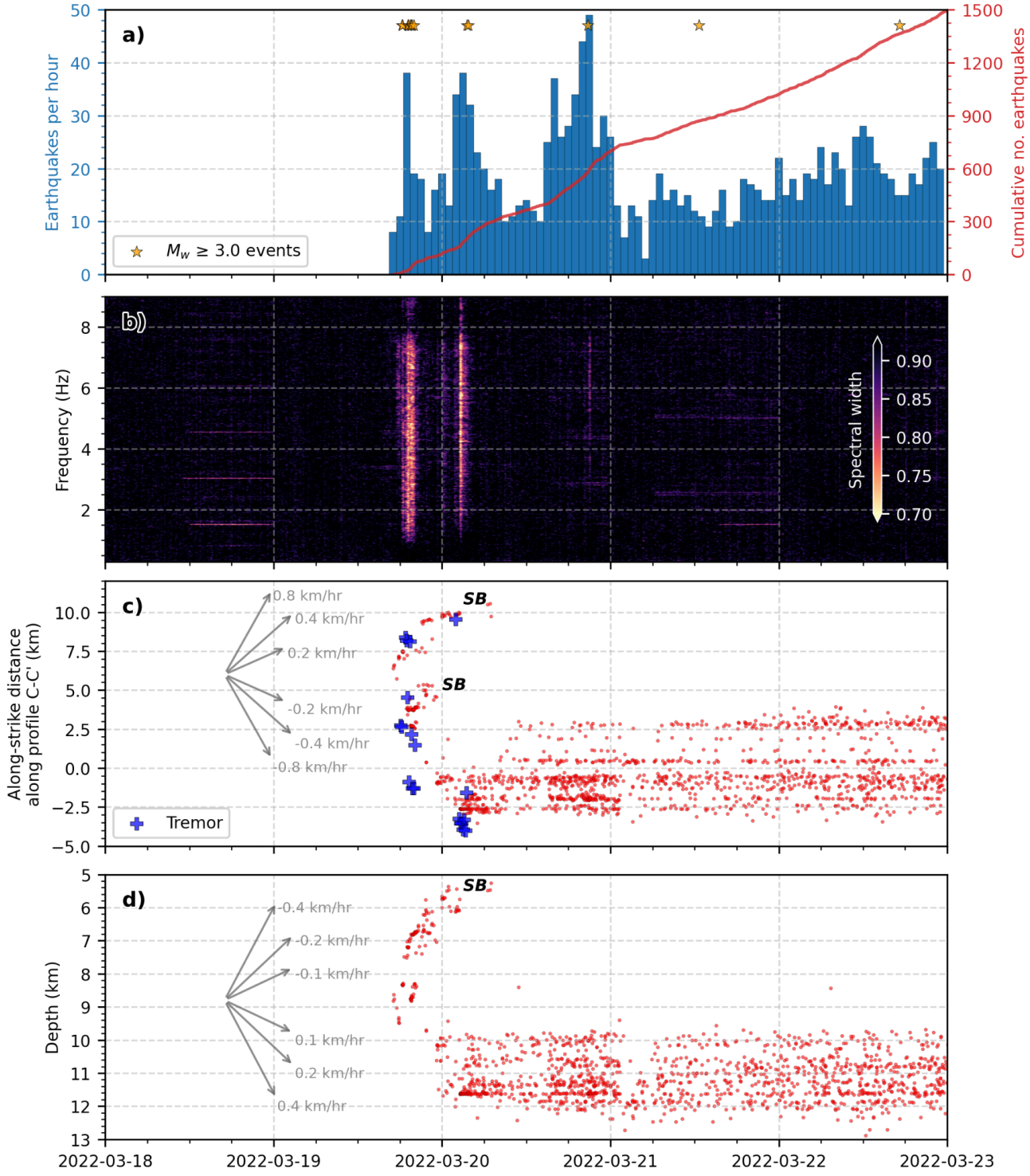

Fig. 5: Onset of the seismic swarm. *(a) Earthquake rate per hour (blue bars), cumulative number of events (red line), and M_w > 3 events (orange stars). (b) Spectral width of the network covariance matrix computed using vertical-component waveforms from permanent seismic stations. A narrow spectral width indicates a coherent, spatially localised source, such as tremor. The lower two panels show the temporal variation of (c) seismicity position along strike (WNW-ESE position; Profile C-C' in Fig. 5, and (d) depth. Grey arrows show indicative lateral and depth migration velocities. Lateral positions of tremor-like bursts are denoted by blue plus symbols in (c) based on maximum likelihood positions from back-projection of smoothed cross-correlation envelopes. "SB" represents the early, upward migrating branches of shallow seismicity.*

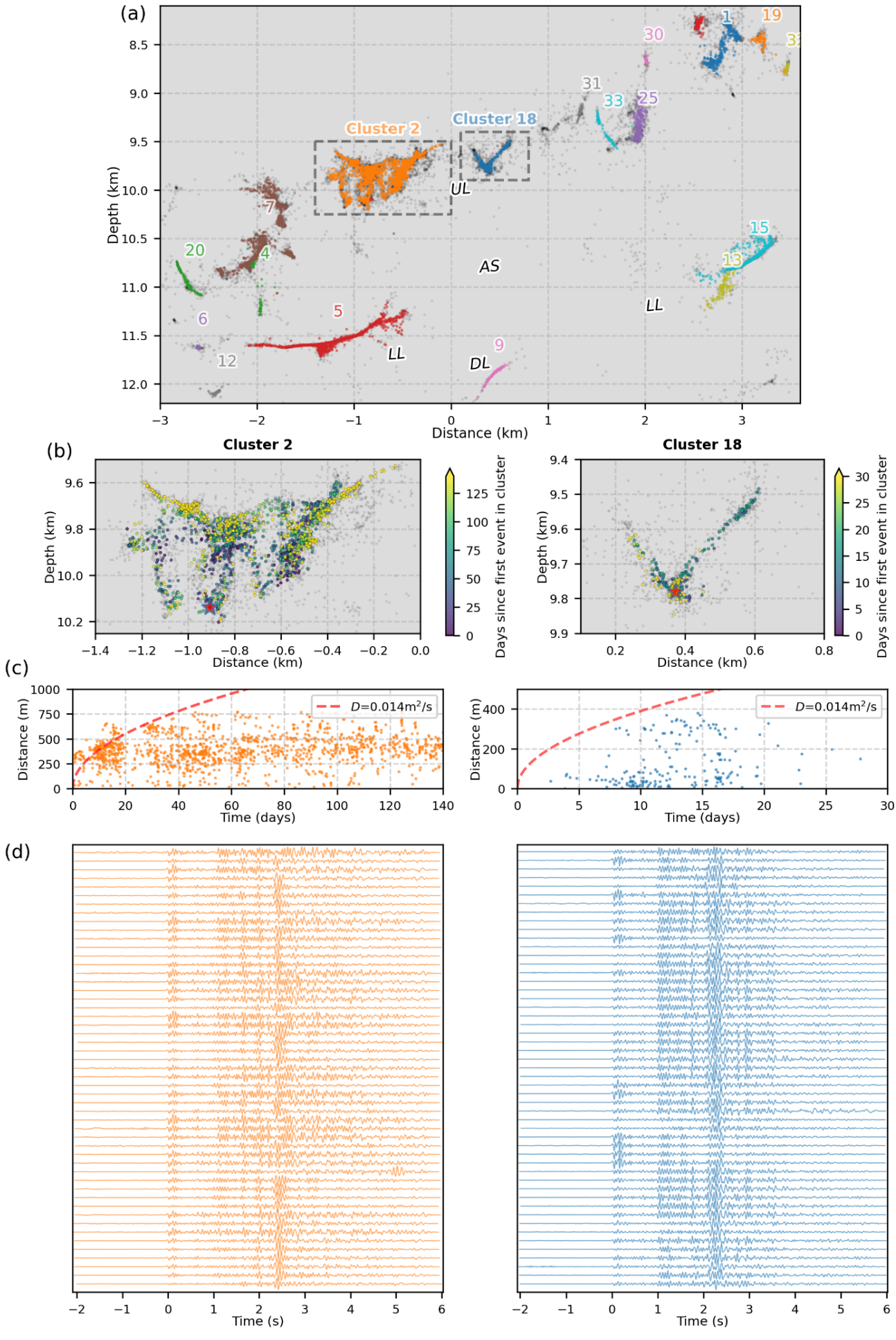
(a)
Depth (km)
Distance (km)
Cluster 2
Cluster 18
UL
AS
LL
DL
(b)
Cluster 2
Cluster 18
Depth (km)
Distance (km)
Days since first event in cluster
(c)
Distance (m)
Time (days)
D=0.014m²/s
(d)
Time (s)

***Fig. 6: Seismic event clustering**. (a) Enlarged view of the main zone of seismicity along the strike-parallel cross-section (Fig. 4d), with events coloured by their waveform correlation-derived cluster. Only clusters with at least 50 events are shown. The panels below show the details of two distinct clusters: 2 (left) and 18 (right). Black dots show the unclustered seismicity. b) Zoomed-in view of these two seismicity clusters, with events coloured by their time relative to the first event in each cluster (red star). c) Events in each cluster are plotted as a function of time and distance relative to the first event in each cluster. The red dashed line represents an approximate fit for the diffusivity of the migrating seismicity front. d) Examples of highly similar waveforms (P-wave cross-correlation coefficient >0.87 with the first earliest in each cluster) in the frequency band 2-40 Hz, with a maximum of 50 events shown for visualisation.*

The highly active swarm had an unusually high *b*-value of ~2.4 (Fig. S13), compared to the global volcanic average of ~1.7[69–71]. Moreover, the total seismic moment released (~10^{16} Nm, or M_w 4.7) is large relative to the intrusion volume (~10^8 m^3) compared to other dike-related VT sequences[70,73] (Fig. 8). These abnormal characteristics are likely due to a fluid-rich environment[71] along the PdC-FZ in the lower crust, with the M_w to intrusion volume scaling slightly tending toward seismicity caused by fluid injection, which has greater seismic efficiency than most volcanic sequences[69] (Fig. 8). The rapid westward and downward migration of seismicity (Fig. 4), which left ~2 km thick aseismic zone ('*AS*') between three seismic lineations ('UL', 'LL', and 'DL'; Fig. 4), may indicate that, following the main dike ascending to the base of the island edifice, a laterally propagating branch of magmatic fluids[71,79,80] may have initiated at the western edge of the vertically-stalled intrusion, at 9-10 km depth[65,73,74] Forward modelling (see *Methods*; Fig. S21), however, shows that such melt branches would need to be small (<10^2 m^3 total volume), so that they do not induce any observable surface deformation. Such thin branches of melt might be consistent with the ultra-thin lineaments of seismicity that we observe (Fig. 4d & 6a). Destabilisation of melt at the western edge of the main dike may be dynamically favourable given the dike's tendency to lean to the west in our ensemble of geodetic solutions (Figs. 4 & S7-S9). We cannot rule out these branches of melt intermixing with fluids, nor can we exclude vertical fluid ascent from the westward-tilting deeper parts of the dike (Fig. 7), or a combination of both lateral and vertical transport. Some seismicity clusters, such as Clusters 2, 7, and 18 (Fig. 6; Movie S1), show complex fracture-like geometries and an upward migrating front over weeks to months with slow diffusivity (~0.001-0.002 m^2/s), suggesting long-lived upward fluid migration along propagating fractures[75] in the PdC-FZ.

Overall, lacking evidence for a substantial laterally propagating melt intrusion in AS, between LL and UL, we propose that fluid pore pressure increases, driven by thermal pressurisation[76], small channels of melt, and magma devolatilisation[77–80], triggered the main seismicity. The PdC-FZ likely facilitated fluid channelling[81] through the lowermost crust near the crust-mantle boundary. Lateral melt branching, exsolution and subsequent devolatilisation, likely increased magma viscosity[4,82,83], helping the dike to stall ~1.6 km below the surface. The resulting static stress change led to the observed left-lateral seismogenic shear along the PdC-FZ, rotated by 90° with respect to the background right-lateral motion[21,22,26,30–33,35,44] (Figs. 1a, 2, 4a). Shear dilatancy effects from an overpressured magma in a relatively weak background stress field may have also contributed to the focal mechanism rotation[13,15,77,84].

Although strongly required by the geodetic data and ACF results, a near-vertical dike opening in a matter of days from 26 km up to 1.6 km depth is an unusual aspect of the 2022 São Jorge unrest. However, magmatic intrusions propagating rapidly at ~0.1-1.0 m/s[59–62], with partial or total aseismicity, especially at mantle depths, are not without precedence[57,59,63]. We infer that because the dike intruded into a mature fault zone, few new fractures had to be created, leading to aseismic Mode-I opening, possibly accompanied by devolatilisation and shear dilatancy at the dike tip[62,63] . Alternatively, the longer-term GNSS deformation transients at far-field stations (e.g., AZTP on Pico, ENAO, Graciosa, and to a lesser extent QEMD on São Jorge; Fig S1) may indicate that the shallower and deeper parts of the modelled dike deformed on different timescales. In this case, we speculate that the mantle segment deformed more slowly due to its inherently different mechanical properties. Such a vertically segmented dike may be consistent with the ACF imaging results, which imply a bimodal depth distribution in subsurface changes, with clear changes at lag times <8 s and >16 s, but without any apparent changes at intermediate depths. However, we cannot formally quantify such a hypothesis with the available time resolution and accuracy of geodetic observations. Regardless of the exact behaviour at depth, such a stealthy and rapid magma ascent presents a challenge for tracking dike intrusions and forecasting their eruptive potential.

Another remaining issue is that residual horizontal GNSS vectors from our preferred quadrangular diking model at stations on islands to the south (AZTP and PIED on Pico; HORT on Faial) show a consistent eastward trend (Fig. S10), which could indicate a left-lateral shear source. This trend is particularly intriguing given the rotated left-lateral slip of the swarm seismicity. Therefore, we inverted the geodetic data for a sheared dike model (Text S1.1). However, we found that the resulting model unsatisfactorily increases the GNSS and InSAR residuals (Table S2) and results in a physically implausible near-horizontal shear dike located too far north of the seismicity. The observed left-lateral shear residual may reflect transient stress perturbations during magma emplacement, possibly linked to shear dilatancy effects or local stress rotations, that may be physically linked to the rotated focal mechanisms. Alternatively, the shear residual may be due to the differential timescale of opening between the mantle and crustal intrusion segments, as described above. However, the sparse GNSS dataset cannot provide confident constraints on such sources.

Overall, our findings highlight clear volcano-tectonic interactions that are most evident in transtensional environments. The dike intruded oblique to the minimum compressive stress (Fig. 4a), but was guided by the PdC-FZ, acting as a major transtensional rift in the central Azores. The magma intrusion likely targeted a weaker fault segment near the PdC-FZ and P-FZ junction (Fig. 4a). The PdC-FZ, capable of generating M~7[26,35,44] earthquakes, likely exhibits along-strike variations in strength and coupling[85,86]. The seismic swarm, confined to the lowermost crust (Figs. 4 & 6a), possibly marks a rheological transition separating the locked shallow fault from the creeping upper mantle.

Although the dike increased PdC-FZ stress for both left- and right-lateral slip modes (Figs. S17-18), the seismic swarm released only M_w 4.7 of left-lateral slip, leaving the likelihood of a future large earthquake, which would presumably release regional tectonically accumulated right-lateral stress, no less likely. Such major crustal faults in the Azores may result from repeated dike intrusions over time[31,87,88].

Our results suggest that pre-existing faults can have opposing effects on magma propagation. The PdC-FZ facilitated rapid vertical melt ascent, but may also have caused magma to stall by allowing lateral devolatilisation and melt escape, thereby increasing viscosity and reducing pressure within the main intrusion. The Azores thus offers new insights into the interplay between magmatism and seismic cycles.

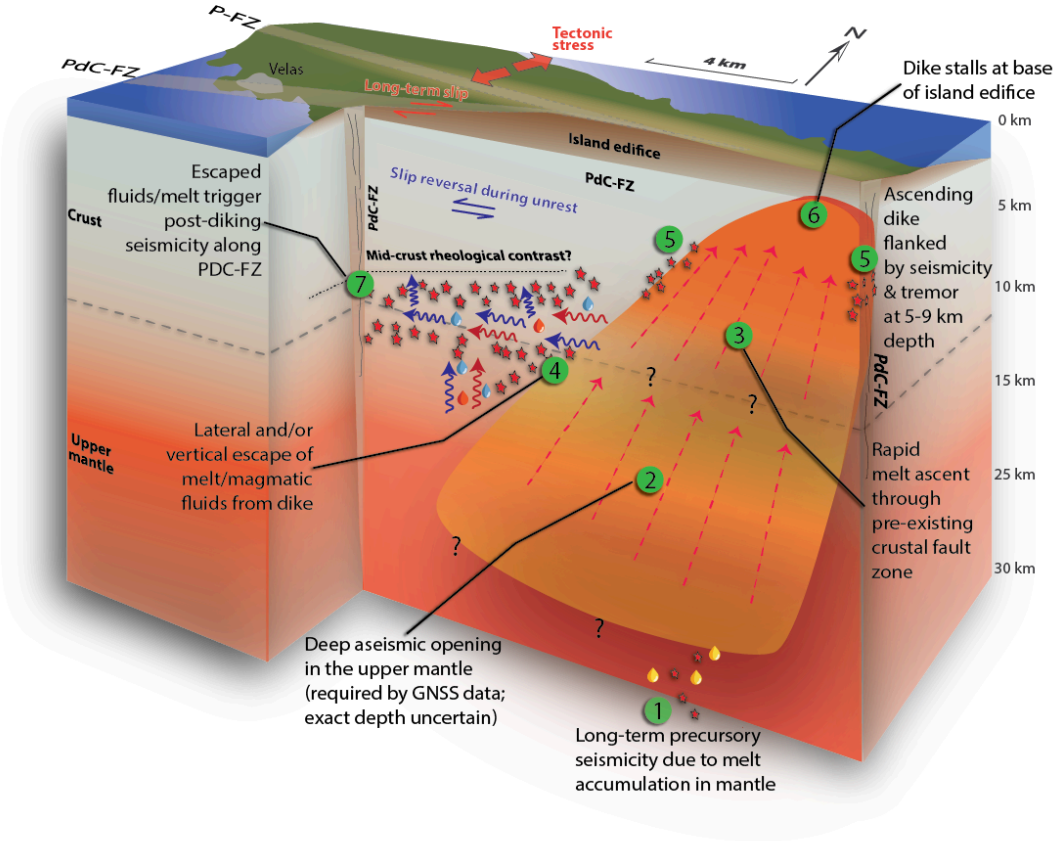

Fig. 7: Interpretation. *a) 3-D schematic view cut along the strike of the PdC-FZ and the intruded dike showing the processes driving the São Jorge seismic-volcanic unrest in 2022. Note the exaggerated width of the dike. Our quadrangular model has uncertainty in resolving the exact depth of the dike. The broken interpreted flow arrows in the dike represent a possible scenario of vertical segmentation of diking dynamics.*

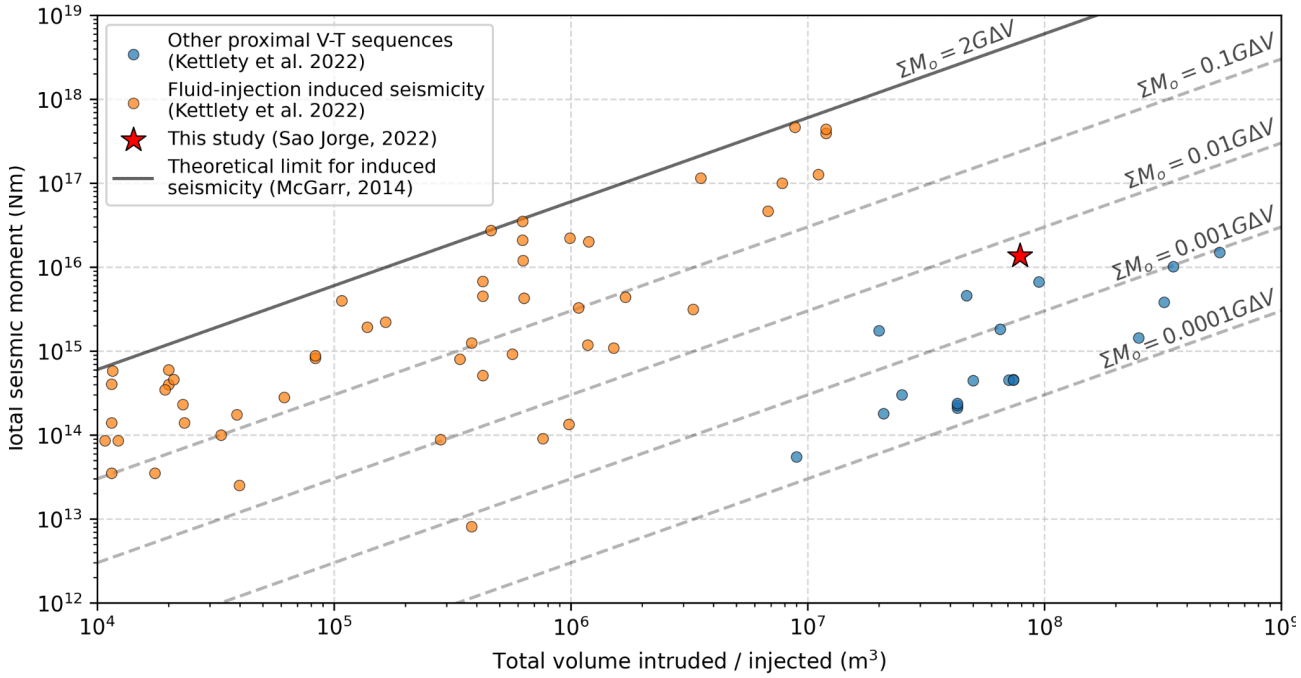

Fig. 8: Global context. *Comparison of intrusion volume versus total seismic moment with other proximal volcano-tectonic (V-T) sequences and fluid injection-induced seismicity*[75]*. Grey dashed lines indicate orders of magnitude smaller scaling of the McGarr*[96] *relationship to account for comparatively lower seismic efficiency in volcanic settings*[75]*. These relationships are depicted with a shear modulus of G = 30 GPa.*

Methods

1. GNSS processing

Daily Solutions

The daily positions of each station were estimated using the GipsyX software package[90], employing the Precise Point Positioning (PPP) strategy[91]. This approach allows for the independent computation of station positions by relying on fixed satellite orbit and clock parameters provided by the Jet Propulsion Laboratory (JPL). To ensure alignment with the latest realisation of the International Terrestrial Reference System, the ITRF2020 reference frame, daily transformation parameters estimated by JPL were applied. For earlier solutions where ITRF2020 transformation parameters were unavailable, existing solutions in ITRF2014 were converted to ITRF2020 using global parameters provided by the International Terrestrial Reference Frame service (https://itrf.ign.fr/).

Time-series Analysis

The long-term motion of each GNSS station was analysed using the Hector software package[92], specifically designed for time series analysis of geodetic data. We modelled the trajectory of each station as a combination of a linear trend (secular motion), seasonal signals (annual and semi-annual variations), and step offsets caused by geophysical or instrumental changes.

Outlier detection and removal were performed as an initial step using an automated approach[93]. To ensure realistic uncertainty estimates for the derived parameters, Hector accounts for temporal correlations in the GNSS time series. A noise model consisting of a power-law component combined with white noise was employed, as this has been shown to accurately represent the noise characteristics of geodetic data. The software estimates not only the linear velocity but also the amplitudes and phase-lags of seasonal signals.

Offsets in the data, resulting from events such as equipment changes, antenna replacements, or geophysical phenomena, were systematically incorporated into the model to ensure accurate estimation of the motion for all stations. For the deformation caused by the dike intrusion, we computed offsets to quantify the sudden displacements observed at the start of the swarm on 19 March 2022. To isolate these displacements, one week of GNSS data around this epoch was excluded from the analysis for all stations. This exclusion minimised the influence of short-term noise and allowed for the precise computation of the deformation signals related to the dike intrusion.

2. Satellite radar interferometry (InSAR) processing

InSAR displacement measurements are obtained by analysing phase differences between radar images acquired by the Sentinel-1A satellite, which are then utilised to generate displacement maps, also known as interferograms[94]. At São Jorge, we processed descending (track orbit number 082) and ascending (track orbit number 002) interferograms using the Hybrid Pluggable Processing Pipeline[95]. We analysed all Sentinel-1A data from 2022-01-01 to 2022-07-31, approximately three months before and after the onset of the unrest. Sentinel-1A images were processed at a multilook factor of 10 pixels in range and 2 pixels in azimuth, resulting in a pixel spacing of about 40 m. Topography phase contributions were removed using the COPERNICUS GLO-30 Global Digital Elevation Model (https://portal.opentopography.org/raster?opentopoID=OTSDEM.032021.4326.3). Residual differential phase interferograms were spatially filtered using a Goldstein filter with 0.6 strength to reduce the impact of decorrelation during phase unwrapping. Also, to minimise negative impacts during phase unwrapping, pixels located in the sea were masked to zero using a fine-resolution coastline. Unwrapping was performed using a minimum-cost flow algorithm. All interferograms were cropped to a common area and georeferenced to the UTM zone 26S coordinate system.

3. Seismic catalogue and relocation

Seismic waveform data

There are two permanent seismic networks in the Azores (codes: PM, CP), operated by IPMA[96] and CIVISA[97], respectively, with just three stations on São Jorge before the start of the 2022 unrest. On 23 March 2022, just four days after the start of the seismic swarm, 15 temporary short-period seismic stations were installed (code: 3K)[98]. Three temporary broadband stations were installed four days later (code: PM). An additional 10 broadband stations were installed on São Jorge and adjacent islands in June 2022 (code: 8S)[99]. Finally, at the end of August 2022, we deployed six short-period ocean bottom seismometers (OBSs) offshore São Jorge (code: 4U)[100]. In this study, we analyse available seismic data until 18 November 2022, covering the first eight months of the seismic swarm. A timeline of stations is shown in Fig. S12.

Seismic catalogue generation workflow

We developed a fully automated workflow to detect, pick, and associate seismic arrivals. For most of the studied period, we used the EQTransformer convolutional neural network model[101] implemented in SeisBench[102], to detect and pick *P*- and *S*-wave arrivals. The association step was performed using PyOcto[103]. For the OBS deployment period, we found that an existing neural network trained on OBSs[104] yielded many false picks, producing many false associations. Therefore, for this latter period,

we used QuakeMigrate [105], which back-projects characteristic functions of the seismic waveforms to a coherent source, thus implicitly associating picked arrival times with events.

This workflow yielded 18,049 well-located events (maximum azimuthal gap ≤ 220°; ≥8 arrival times) relocated in an initial velocity model based on Rayleigh wave ellipticities recorded at PM.ROSA in the west of São Jorge[47] (Fig. S18). We generated 5,000 random realisations of this starting model, perturbing velocities (up to 2 km/s) and layer thicknesses (ensuring a minimum thickness of 0.5 km and maximum thickness of 4 km), jointly inverting for velocity structure and hypocentres[106–108]. We chose the best-fitting output model as our preferred, minimum 1-D velocity structure (Fig. S18).

NLL-SSST-coherence relocation method

Initial locations using our inverted 1-D velocity model (Fig. S18) reveal a highly clustered swarm; however, the relatively large uncertainty in the absolute hypocentre positions (median depth uncertainty of 430 m) indicates that greater precision is needed. Moreover, the evolving station density during the 2022 São Jorge seismic swarm, with sparse station coverage for the first few days, necessitates a joint earthquake relocation approach that couples station corrections and relative locations between the later and earlier periods. We, therefore, used a new, multi-scale high-precision method, *NLL-SSST-coherence*[109,110], which combines source-specific station travel-time corrections (SSSTs) to account for 3-D velocity heterogeneity, with the stacking of hypocentre probability density functions based on inter-event waveform coherence to improve smaller-scale relative location. We computed inter-event waveform coherency using a 2-40 Hz bandpass filter.

The workflow of NLL-SSST-coherence comprises a two-step process. First, SSSTs to our best-fitting 1-D velocity model (Fig. S18) are developed iteratively over collapsing length scales, using well-constrained events with at least 15 arrival times. Next, assuming that highly similar waveforms for two events recorded at the same station imply the events are nearly co-located, we measure inter-event waveform coherency at multiple stations as a weight to combine and stack the location probability density functions from the NLL-SSST relocations. This approach effectively reduces stochastic noise in travel-time data, greatly improving the location precision of target events. The practical advantages of this approach are that it only requires waveforms for a few stations and is computationally fast compared to other higher-precision relative location algorithms, such as hypoDD and GrowClust, because differential arrival time measurements do not need to be computed. NLL-SSST-coherence yields high location precision across multiple scales, leading to a different interpretation of seismicity patterns than with methods that focus on fine-scale precision[109]. NLL-SSST-coherence has been applied to volcano-tectonic seismicity in other areas[111].

Magnitudes

We computed a new magnitude scale including station corrections by inverting observed amplitudes of the São Jorge seismicity using least-squares[112]. This computation yielded the following ML equation:

$$M_L = log(A) + 0.656\, log(r/17) + 0.00948 log(r - 17) + 2 + C$$

where A is the Wood-Anderson simulated horizontal-component amplitude in mm, r is the hypocentral distance in km, and *C* represents inverted station corrections.

We also computed M_w using S_H-wave spectra[113,114]. We found that compared to *P*-wave spectra, M_w estimates from S_H-wave spectra yielded far more observations per station (Fig. S14), especially at lower magnitudes, resulting in network-averaged Mw values with higher stability. The comparison between Mw and ML is shown in Fig. S15 (Mw = 0.63ML + 0.91).**Frequency-magnitude relationships**

Caution is needed when interpreting *b*-values from frequency-magnitude distributions using local magnitude (M_L) scales of low-magnitude seismic sequences[115–120]. These studies show that moment magnitude (M_w) gives more accurate b-value estimates. We computed *b*-values for both M_w and M_L, using magnitude of completeness (M_c) values for each one approximated using the boundary-value-stability method[55,69,118,119]. Our results show a similar discrepancy between M_w and M_L (Fig. S13). Therefore, we prefer to use *b*-values from moment magnitudes.

Focal mechanisms

We computed focal mechanisms using Bayesian inversion of first-motion polarity data[122]. All solutions were best fit by double-couple mechanisms. An example solution is shown in Fig. S16.

4. Mechanical modelling of surface displacement observations

The surface displacements observed by the GNSS network and Sentinel-1A interferograms show evidence of a major island axis elongated dilatation source in the central-west area of São Jorge. This pattern is characteristic of magmatic intrusions, typically a nearly vertical dike. To quantify the dimensions and magma volume associated with this intrusive pattern, we utilised a Bayesian 3D Mixed Boundary Element Method (BEM) inversion[123]. The model assumes that the island edifice and upper crust are homogeneous, isotropic and behave elastically with a Young's modulus of 5 GPa and a Poisson's ratio of 0.25. The 3D BEM method is a flexible numerical approach accounting for topography/bathymetry and non-planar dilatant cracks (e.g., quadrangles). The weights of the three types of observations were normalised in the inversion. This weighting approach prevents biasing the

inversion to the denser InSAR data, ensuring that each dataset contributes equally to the model solution[124].

To account for a realistic topography, we created a blended topography and bathymetry model at 100 m spatial resolution, combining the GLO30 COPERNICUS model for the island's topography and the 2023 version of the EMODnet bathymetry model for the Azores (EMODnet DTM 2022).

We explore models of planar quadrangular intrusions allowing for tilted (inwards or outwards) crack boundaries along depth. First, the inversion explores nonlinear geometry parameters, followed by the solution of the opening, which satisfies constant overpressure, by linear inversion. Note that a single magma overpressure parameter controls the dike opening pattern. This physically realistic assumption produces spatially smooth opening distributions, independent of the chosen crack mesh discretisation, and avoids setting up a linear inversion regularisation smoothing parameter (typical for kinematic inversions).

The inversion iteratively explores a large set of model parameters that describe the dike intrusion position, orientation and dimensions by generating forward models optimised by a neighbourhood inversion algorithm[125,126]. See Table S1 for a full description of these geometric parameters. These models minimise the misfit with the observed displacements between 15 and 21 March 2022. To carry out the inversions efficiently, the spatial resolution of the surface displacement maps was reduced using a quadtree partition approach, with a minimum average quadrant size of 8 pixels and a maximum of 128 pixels. To subdivide the quadrants, two conditions were specified: displacement variance and displacement thresholds, both of 0.03 m. These parameters result in the selection of 698 and 702 points for the descending and ascending interferograms, respectively. We used all three components of the GNSS vectors. During the inversion, the weights of the three types of observations were normalised to avoid results being dominated by a single dataset.

Convergence of the inversion was assessed by monitoring the evolution of model misfit and the spread of accepted solutions. The inversion was terminated after 250 iterations, when the model cost fell below 750 and was stable for the last 100 iterations, indicating a stable inversion (Figs. S9 & S22). The posterior distributions of model parameters (Figs. S7-S9) show well-constrained values for dike strike, dip, and opening, with broader uncertainty in depth extent. This convergence behaviour supports the robustness of the inferred quadrangular intrusion geometry.

We also explored a wide range of other models, the results of which are detailed in Text S1.

Forward modelling of a laterally-propagating dike

To explore the scenario of a laterally migrating dike, we forward-modelled intrusion scenarios through the seismicity region using a range of dike opening models with random (20,000 samples)

geometries/sizes using parameters from the solution space of the geodetic inversion. We found that most models produce a surface displacement signal that would be resolvable using the GNSS network in São Jorge or InSAR data, but we do not observe this (Fig. S21). Only very small intrusions, with <100-to-1000 m^3 of magma, would have been missed by GNSS (<1 mm) and InSAR (<1 cm). Therefore, we can likely rule out laterally propagating dike fingers hundreds of metres to ~2 km wide in depth.

5. Tremor detection

To detect tremor-like bursts of seismicity, we used the covseisnet software package[134,135]. This method exploits the coherence of tremor signals across the network, which is computed in the form of an array covariance matrix. Long-duration sources of coherent seismic energy are given by a low spectral width value of the array covariance matrix (Fig. 5b). We pre-processed vertical component data from permanent seismic stations (PM.PMAN, PM.ROSA, PM.SRBC, PM.PID, PM.HOR, PM.PCED, PM.PGRA, PM.PICO, PM.PCAN, PM.PPNO, CP.PAMA, PM.PSCM) with spectral whitening in 50-second windows followed by a temporal normalization to minimize the impact of large, individual earthquakes. We average the network covariance matrix into 20-minute-long windows, overlapping by 50%. In each window, cross-correlation functions are filtered in the 0.5–9 Hz band of interest. Then, a grid search determines the set of inter-station time delays that maximise the stacked correlation function envelopes at zero lag. To determine the tremor source locations (Fig. 5c), we back-project these cross-correlation time-shifts in the *S*-wave source-specific travel-time models derived from the fine-scale earthquake relocation workflow.

6. Auto-correlation imaging

The ACF approach has been successfully used to image temporal variations in subsurface structure beneath volcanic regions[127–129]. The phase autocorrelation method is not biased by high-amplitude features such as earthquakes and thus does not require pre-processing (e.g., time-domain normalisation and spectral whitening) to remove these features[130–132]. We tested different frequency bands and found that the 1.0-3.0 Hz band gave the most stable results, and is lower than most of the radiation from events of the seismic swarm. We also tested three different stacking windows, with and without overlap, and obtained consistent results. The ACFs were computed as 3-day linear stacks with a 2-day overlap.

Acknowledgements

We are grateful to the UK Ocean Bottom Instrument Consortium (OBIC)[133] (https://obs.ac.uk) and SEIS-UK (https://seis-uk.le.ac.uk/) teams for providing the instrumentation and installation services. S.P.H. is funded by a Natural Environment Research Council Independent Research Fellowship (UKRI184; NE/B000184/1). A.M.G.F, R.R., and N.M. received urgency funding from the Natural Environment Research Council (NE/X006298/1). A.M.G.F. also acknowledges funding from the European Research Council (101001601). This work was also supported by Portuguese FCT/MCTES through national funds (PIDDAC), namely through projects GEMMA (PTDC/CTA-GEO/2083/2021), RESTLESS (PTDC/CTA-GEF/6674/2020, DOI: 10.54499/PTDC/CTA-GEF/6674/2020), UIDB/04683/2020 (DOI: 10.54499/UIDB/04683/2020), and UIDP/04683/2020 (DOI: 10.54499/UIDP/04683/2020), and the Spanish Ministry of Science, Innovation and Universities VolcaMotion project (*Proyecto* PID2022-139159NB-I00 *financiado por MCIN/AEI/10.13039/501100011033/ y por FEDER Una manera de hacer Europa*). A.P. acknowledges the CEEC Institutional contract funded by FCT (DOI: 10.54499/CEECINST/00024/2021/CP2780/CT0003). The Portuguese Navy (Marinha Portuguesa) is acknowledged for providing critical support in the deployment and recovery of the OBS network; we particularly thank the captain and crews of NRPs *António Enes* and *Sines*. The Azores Government, through its Fundo Regional para a Ciência, is also acknowledged for its financial support to harbour operations during the deployment and recovery of the OBS network. We thank Paula Lourinho, Filipe Porteiro and Octávio Melo from OKEANOS, University of the Azores, Sandra Sequeira from Observatório Príncipe Alberto do Mónaco (IPMA) in Faial, José Silva (Serviço de Ambiente e Ação Climática de São Jorge / Parque Natural de São Jorge) and Miguel Mendonça (Municipality of Angra do Heroísmo), for crucial logistics support for both the OBS and land deployments. We thank the CAD team from CIVISA for collecting and processing seismic data. We thank Luis Matias (IDL and the University of Lisbon) and Thomas Boulesteix (IPNA-CSIC) for fruitful discussions. We are very grateful to Valérie Cayol and two anonymous reviewers for taking the time to provide insightful comments on our original manuscript.

Data and Code availability

Seismic waveform data from the PM network[96] are available from the IPMA FDSN webservices client at http://ceida.ipma.pt/. Waveform data from temporary networks 8S[99] and 4U[100] are archived at the Earthscope Data Management Center (http://ds.iris.edu) and are under embargo until 2026-01-01.

Our seismicity catalogue and 1-D layered velocity model are available from a Zenodo repository[134].

The Sentinel-1A IW SLCs and satellite orbits files used in this study are provided by the European Space Agency (ESA). Files are publicly available through the Alaska Satellite Facility (ASF) Data Search Vertex (https://search.asf.alaska.edu). Bathymetry data around the Azores from the EMODnet Digital Bathymetry [135], while topography on land was obtained from the COPERNICUS GLO-30 Global Digital Elevation Model (https://portal.opentopography.org/raster?opentopoID=OTSDEM.032021.4326.3).

The GNSS daily files for the stations used in this study are available at the Portuguese GNSS National Repository managed by the Collaboratory for Geosciences (https://glass.c4g-pt.eu/), maintained with the support of EPOS (European Plate Observing System) (https://www.epos-eu.org/). The analysed stations belong to different networks: QEMD, HORT, PIED, AZTP, AZGR, TERC are part of the REPRAA network (https://repraa.azores.gov.pt/); ENAO is part of the IGS network (https://igs.org); and VLAZ and PAGU are part of the C4G network (https://glass.c4g-pt.eu/).

Geodetic inverse models were conducted using the DefVolc software, which is available online at http://opgc.fr/defvolc. Displacements, strains and stresses from triangular dislocations were computed using cutde (https://github.com/tbenthompson/cutde).

Movie S1 was made with the Sparrow software of the Pyrocko package.

Author contributions

Conceptualization: SPH, PJG, AMGF, RSR, NM

Methodology: SPH, PJG, AL, AMGF, RSR

Software: SPH, PJG, AL, GS

Validation: SPH, PJG, GS

Formal analysis: SPH, PJG, AL, RSR

Investigation: SPH, PJG, AMGF, RSR, NM, GS, NAF, JF, RF, AP, MT, VM, RS, WS, AM, FC, RM, MM, GP

Data Curation: SPH, AMGF, NAD, RF, MT, VM, RS, AP, WS, AM, FC, RM

Writing - Original Draft: SPH, PJG, AMGF, RSR, NM

Writing - Review & Editing: SPH, PJG, AL, AMGF, RSR, NM, GS, NAD, JF, RF, AP, SC, RM, VM, WS, RM, GP

Visualisation: SPH, PJG, AL, RSR, GS

Supervision: AMGF

Project administration: SPH, PJG, AMGF

Funding acquisition: AMGF, RSR, NM, RF, PJG, RM, SC, NAD

References

1. Moran, S. C., Newhall, C. & Roman, D. C. Failed magmatic eruptions: late-stage cessation of magma ascent. *Bull. Volcanol.* **73**, 115–122 (2011).
2. Rubin, A. M. Dike-induced faulting and graben subsidence in volcanic rift zones. *J. Geophys. Res. Solid Earth* **97**, 1839–1858 (1992).
3. Rivalta, E., Taisne, B., Bunger, A. P. & Katz, R. F. A review of mechanical models of dike propagation: Schools of thought, results and future directions. *Tectonophysics* **638**, 1–42 (2015).
4. Lejeune, A. M., Bottinga, Y., Trull, T. W. & Richet, P. Rheology of bubble-bearing magmas. *Earth Planet. Sci. Lett.* **166**, 71–84 (1999).
5. Gaffney, E. S., Damjanac, B. & Valentine, G. A. Localization of volcanic activity: 2. Effects of pre-existing structure. *Earth Planet. Sci. Lett.* **263**, 323–338 (2007).
6. Gudmundsson, A. Form and dimensions of dykes in eastern Iceland. *Tectonophysics* **95**, 295–307 (1983).
7. Sigmundsson, F. *et al.* Fracturing and tectonic stress drives ultrarapid magma flow into dikes. *Science* **0**, eadn2838 (2024).
8. Ziv, A., Rubin, A. M. & Agnon, A. Stability of dike intrusion along preexisting fractures. *J. Geophys. Res. Solid Earth* **105**, 5947–5961 (2000).
9. Maccaferri, F., Rivalta, E., Passarelli, L. & Aoki, Y. On the mechanisms governing dike arrest: Insight from the 2000 Miyakejima dike injection. *Earth Planet. Sci. Lett.* **434**, 64–74 (2016).
10. Bangs, N. L. B., Shipley, T. H., Moore, J. C. & Moore, G. F. Fluid accumulation and channeling along the northern Barbados Ridge decollement thrust. *J. Geophys. Res. Solid Earth* **104**, 20399–20414 (1999).
11. Caricchi, L., Townsend, M., Rivalta, E. & Namiki, A. The build-up and triggers of volcanic eruptions. *Nat. Rev. Earth Environ.* **2**, 458–476 (2021).
12. Ross, Z. E., Cochran, E. S., Trugman, D. T. & Smith, J. D. 3D fault architecture controls the dynamism of earthquake swarms. *Science* **368**, 1357–1361 (2020).
13. Roman, D. C. Numerical models of volcanotectonic earthquake triggering on non-ideally

oriented faults. *Geophys. Res. Lett.* **32**, (2005).

14. Manga, M. & Brodsky, E. Seismic Triggering of Eruptions in the Far Field: Volcanoes and Geysers. *Annu. Rev. Earth Planet. Sci.* **34**, 263–291 (2006).
15. Roman, D. C. & Heron, P. Effect of regional tectonic setting on local fault response to episodes of volcanic activity. *Geophys. Res. Lett.* **34**, (2007).
16. Toda, S., Stein, R. S. & Sagiya, T. Evidence from the ad 2000 Izu islands earthquake swarm that stressing rate governs seismicity. *Nature* **419**, 58–61 (2002).
17. White, R. S., Edmonds, M., Maclennan, J., Greenfield, T. & Agustsdottir, T. Melt movement through the Icelandic crust. *Philos. Trans. R. Soc. Math. Phys. Eng. Sci.* **377**, 20180010 (2019).
18. Wilding, J. D., Zhu, W., Ross, Z. E. & Jackson, J. M. The magmatic web beneath Hawai'i. *Science* **379**, 462–468 (2023).
19. Einarsson, P., Hjartardóttir, Á. R., Hreinsdóttir, S. & Imsland, P. The structure of seismogenic strike-slip faults in the eastern part of the Reykjanes Peninsula Oblique Rift, SW Iceland. *J. Volcanol. Geotherm. Res.* **391**, 106372 (2020).
20. Drymoni, K., Browning, J. & Gudmundsson, A. Volcanotectonic interactions between inclined sheets, dykes, and faults at the Santorini Volcano, Greece. *J. Volcanol. Geotherm. Res.* **416**, 107294 (2021).
21. Trippanera, D. *et al.* Relationships between tectonics and magmatism in a transtensive/transform setting: An example from Faial Island (Azores, Portugal). *GSA Bull.* **126**, 164–181 (2014).
22. Hildenbrand, A. *et al.* Multi-stage evolution of a sub-aerial volcanic ridge over the last 1.3 Myr: S. Jorge Island, Azores Triple Junction. *Earth Planet. Sci. Lett.* **273**, 289–298 (2008).
23. DeMets, C., Gordon, R. G. & Argus, D. F. Geologically current plate motions. *Geophys. J. Int.* **181**, 1–80 (2010).
24. Mendes, V. B. *et al.* Present-day deformation in São Jorge Island, Azores, from episodic GPS measurements (2001–2011). *Adv. Space Res.* **51**, 1581–1592 (2013).
25. Marques, F. O., Hildenbrand, A. & Hübscher, C. Evolution of a volcanic island on the shoulder of

an oceanic rift and geodynamic implications: S. Jorge Island on the Terceira Rift, Azores Triple Junction. *Tectonophysics* **738–739**, 41–50 (2018).

26. Lourenço, N. *et al.* Morpho-tectonic analysis of the Azores Volcanic Plateau from a new bathymetric compilation of the area. *Mar. Geophys. Res.* **20**, 141–156 (1998).
27. Borges, J. F., Bezzeghoud, M., Buforn, E., Pro, C. & Fitas, A. The 1980, 1997 and 1998 Azores earthquakes and some seismo-tectonic implications. *Tectonophysics* **435**, 37–54 (2007).
28. Ekström, G., Nettles, M. & Dziewoński, A. M. The global CMT project 2004–2010: Centroid-moment tensors for 13,017 earthquakes. *Phys. Earth Planet. Inter.* **200–201**, 1–9 (2012).
29. Frietsch, M., Ferreira, A., Vales, D. & Carrilho, F. On the robustness of seismic moment tensor inversions for mid-ocean earthquakes: the Azores archipelago. *Geophys. J. Int.* **215**, 564–584 (2018).
30. Madeira, J. & Ribeiro, A. Geodynamic models for the Azores triple junction: A contribution from tectonics. *Tectonophysics* **184**, 405–415 (1990).
31. Silva, P. F. *et al.* Palaeomagnetic study of a subaerial volcanic ridge (São Jorge Island, Azores) for the past 1.3 Myr: evidence for the Cobb Mountain Subchron, volcano flank instability and tectonomagmatic implications. *Geophys. J. Int.* **188**, 959–978 (2012).
32. Neves, M. C., Miranda, J. M. & Luis, J. F. The role of lithospheric processes on the development of linear volcanic ridges in the Azores. *Tectonophysics* **608**, 376–388 (2013).
33. Moreira, M. A., Geoffroy, L. & Pozzi, J. P. Magma flow pattern in dykes of the Azores revealed by anisotropy of magnetic susceptibility. *J. Geophys. Res. Solid Earth* **120**, 662–690 (2015).
34. Marques, F. O., Catalão, J. C., DeMets, C., Costa, A. C. G. & Hildenbrand, A. GPS and tectonic evidence for a diffuse plate boundary at the Azores Triple Junction. *Earth Planet. Sci. Lett.* **381**, 177–187 (2013).
35. Madeira, J., Brum da Silveira, A., Hipólito, A. & Carmo, R. Chapter 3 Active tectonics in the central and eastern Azores islands along the Eurasia–Nubia boundary: a review. *Geol. Soc. Lond. Mem.* **44**, 15–32 (2015).

36. Miranda, J. M., Luis, J. F., Lourenço, N. & Goslin, J. Distributed deformation close to the Azores Triple "Point". *Mar. Geol.* **355**, 27–35 (2014).

37. Marzoli, A. *et al.* Time-Dependent Evolution and Source Heterogeneities of Ocean Island Basalts from a Weak Plume, São Jorge, Azores. *J. Petrol.* egae122 (2024) doi:10.1093/petrology/egae122.

38. Forjaz, V. H. & Weston, F. S. Volcanic activity in the Azores. Report for 1959–1964. *Bull. Volcanol.* **31**, 261–266 (1967).

39. Zanon, V. & Viveiros, F. A multi-methodological re-evaluation of the volcanic events during the 1580 CE and 1808 eruptions at São Jorge Island (Azores Archipelago, Portugal). *J. Volcanol. Geotherm. Res.* **373**, 51–67 (2019).

40. Gaspar, J. L. *et al.* Chapter 4 Earthquakes and volcanic eruptions in the Azores region: geodynamic implications from major historical events and instrumental seismicity. *Geol. Soc. Lond. Mem.* **44**, 33–49 (2015).

41. Fontiela, J., Sousa Oliveira, C. & Rosset, P. Characterisation of Seismicity of the Azores Archipelago: An Overview of Historical Events and a Detailed Analysis for the Period 2000–2012. in *Volcanoes of the Azores: Revealing the Geological Secrets of the Central Northern Atlantic Islands* (eds. Kueppers, U. & Beier, C.) 127–153 (Springer, Berlin, Heidelberg, 2018). doi:10.1007/978-3-642-32226-6_8.

42. Silva, R., Carmo, R. & Marques, R. Characterization of the tectonic origins of historical and modern seismic events and their societal impact on the Azores Archipelago, Portugal. in *Characterization of Modern and Historical Seismic–Tsunamic Events, and Their Global–Societal Impacts* (eds. Dilek, Y., Ogawa, Y. & Okubo, Y.) 0 (Geological Society of London, 2021). doi:10.1144/SP501-2019-106.

43. Machado, F. O terramoto de S. Jorge, em 1757. *Açoreana* **4**, 311–324 (1949).

44. Madeira, J. & Brum da Silveira, A. Active tectonics and first paleoseismological results in Faial, Picoand S. Jorge islands (Azores, Portugal). (2003).

45. Suarez, E. D. *et al.* São Jorge's Volcano-Tectonic Unrest in 2022: A Joint Interpretation Through

GNSS and Fully Automated Seismic Analysis. *Pure Appl. Geophys.* (2024) doi:10.1007/s00024-024-03612-y.

46. Spieker, K., Rondenay, S., Ramalho, R., Thomas, C. & Helffrich, G. Constraints on the structure of the crust and lithosphere beneath the Azores Islands from teleseismic receiver functions. *Geophys. J. Int.* **213**, 824–835 (2018).
47. Ferreira, A. M. G., Marignier, A., Attanayake, J., Frietsch, M. & Berbellini, A. Crustal structure of the Azores Archipelago from Rayleigh wave ellipticity data. *Geophys. J. Int.* **221**, 1232–1247 (2020).
48. Bondár, I. & Storchak, D. Improved location procedures at the International Seismological Centre: Improved location procedures at the ISC. *Geophys. J. Int.* **186**, 1220–1244 (2011).
49. Chamberlain, C. J. *et al.* EQcorrscan: Repeating and Near-Repeating Earthquake Detection and Analysis in Python. *Seismol. Res. Lett.* **89**, 173–181 (2017).
50. Petersen, G. M., Niemz, P., Cesca, S., Mouslopoulou, V. & Bocchini, G. M. Clusty, the waveform-based network similarity clustering toolbox: concept and application to image complex faulting offshore Zakynthos (Greece). *Geophys. J. Int.* **224**, 2044–2059 (2021).
51. Schimmel, M. *et al.* Seismic Noise Autocorrelations on Mars. *Earth Space Sci.* **8**, e2021EA001755 (2021).
52. Zanon, V., Pimentel, A., Auxerre, M., Marchini, G. & Stuart, F. M. Unravelling the magma feeding system of a young basaltic oceanic volcano. *Lithos* **352–353**, 105325 (2020).
53. Zanon, V., Silva, R. & Goulart, C. The crust-mantle transition beneath the Azores region (central-north Atlantic Ocean). *Contrib. Mineral. Petrol.* **178**, 50 (2023).
54. Leva, C., Rümpker, G., Link, F. & Wölbern, I. Mantle earthquakes beneath Fogo volcano, Cape Verde: Evidence for subcrustal fracturing induced by magmatic injection. *J. Volcanol. Geotherm. Res.* **386**, 106672 (2019).
55. Torres-González, P. A. *et al.* Unrest signals after 46 years of quiescence at Cumbre Vieja, La Palma, Canary Islands. *J. Volcanol. Geotherm. Res.* **392**, 106757 (2020).
56. Greenfield, T. *et al.* Deep long period seismicity preceding and during the 2021 Fagradalsfjall

eruption, Iceland. *Bull. Volcanol.* **84**, 101 (2022).

57. Hudson, T. S. *et al.* Deep crustal melt plumbing of Bárðarbunga volcano, Iceland. *Geophys. Res. Lett.* **44**, 8785–8794 (2017).
58. del Fresno, C. *et al.* Magmatic plumbing and dynamic evolution of the 2021 La Palma eruption. *Nat. Commun.* **14**, 358 (2023).
59. Roman, D. C. & Cashman, K. V. Top–Down Precursory Volcanic Seismicity: Implications for 'Stealth' Magma Ascent and Long-Term Eruption Forecasting. *Front. Earth Sci.* **6**, (2018).
60. Yamaoka, K., Kawamura, M., Kimata, F., Fujii, N. & Kudo, T. Dike intrusion associated with the 2000 eruption of Miyakejima Volcano, Japan. *Bull. Volcanol.* **67**, 231–242 (2005).
61. Ebinger, C. J. *et al.* Capturing magma intrusion and faulting processes during continental rupture: Seismicity of the Dabbahu (Afar) rift. *Geophys. J. Int.* **174**, 1138–1152 (2008).
62. Keir, D. *et al.* Evidence for focused magmatic accretion at segment centers from lateral dike injections captured beneath the Red Sea rift in Afar. *Geology* **37**, 59–62 (2009).
63. Pallister, J. S. *et al.* Broad accommodation of rift-related extension recorded by dyke intrusion in Saudi Arabia. *Nat. Geosci.* **3**, 705–712 (2010).
64. White, R. S. *et al.* Dynamics of dyke intrusion in the mid-crust of Iceland. *Earth Planet. Sci. Lett.* **304**, 300–312 (2011).
65. Woods, J., Winder, T., White, R. S. & Brandsdóttir, B. Evolution of a lateral dike intrusion revealed by relatively-relocated dike-induced earthquakes: The 2014–15 Bárðarbunga–Holuhraun rifting event, Iceland. *Earth Planet. Sci. Lett.* **506**, 53–63 (2019).
66. Cesca, S. *et al.* Massive earthquake swarm driven by magmatic intrusion at the Bransfield Strait, Antarctica. *Commun. Earth Environ.* **3**, 1–11 (2022).
67. Sigmundsson, F. *et al.* Deformation and seismicity decline before the 2021 Fagradalsfjall eruption. *Nature* **609**, 523–528 (2022).
68. Roberts, N. S., Bell, A. F. & Main, I. G. Are volcanic seismic *b*-values high, and if so when? *J. Volcanol. Geotherm. Res.* **308**, 127–141 (2015).
69. Kettlety, T., Kendall, J. M. & Roman, D. C. Self-Similarity of Seismic Moment Release to Volume

Change Scaling for Volcanoes: A Comparison With Injection-Induced Seismicity. *Geophys. Res. Lett.* **49**, e2022GL099369 (2022).

70. Glazner, A. F. & McNutt, S. R. Relationship Between Dike Injection and b-Value for Volcanic Earthquake Swarms. *J. Geophys. Res. Solid Earth* **126**, e2020JB021631 (2021).
71. Wyss, M., Shimazaki, K. & Wiemer, S. Mapping active magma chambers by b values beneath the off-Ito volcano, Japan. *J. Geophys. Res. Solid Earth* **102**, 20413–20422 (1997).
72. Meyer, K., Biggs, J. & Aspinall, W. A Bayesian reassessment of the relationship between seismic moment and magmatic intrusion volume during volcanic unrest. *J. Volcanol. Geotherm. Res.* **419**, 107375 (2021).
73. Di Luccio, F. *et al.* Seismic signature of active intrusions in mountain chains. *Sci. Adv.* **4**, e1701825 (2018).
74. Wilding, J. D. & Ross, Z. E. Rift Zone Architecture and Inflation-Driven Seismicity of Mauna Loa Volcano. *J. Geophys. Res. Solid Earth* **129**, e2024JB029726 (2024).
75. Schofield, N. J., Brown, D. J., Magee, C. & Stevenson, C. T. Sill morphology and comparison of brittle and non-brittle emplacement mechanisms. *J. Geol. Soc.* **169**, 127–141 (2012).
76. Elsworth, D. & Voight, B. Dike intrusion as a trigger for large earthquakes and the failure of volcano flanks. *J. Geophys. Res. Solid Earth* **100**, 6005–6024 (1995).
77. Roman, D. C. & Cashman, K. V. The origin of volcano-tectonic earthquake swarms. *Geology* **34**, 457–460 (2006).
78. Martens, H. R. & White, R. S. Triggering of microearthquakes in Iceland by volatiles released from a dyke intrusion. *Geophys. J. Int.* **194**, 1738–1754 (2013).
79. Coulon, C. A., Hsieh, P. A., White, R., Lowenstern, J. B. & Ingebritsen, S. E. Causes of distal volcano-tectonic seismicity inferred from hydrothermal modeling. *J. Volcanol. Geotherm. Res.* **345**, 98–108 (2017).
80. Wicks, C. W., Dzurisin, D., Lowenstern, J. B. & Svarc, J. Magma Intrusion and Volatile Ascent Beneath Norris Geyser Basin, Yellowstone National Park. *J. Geophys. Res. Solid Earth* **125**, e2019JB018208 (2020).

81. Díaz-Moreno, A. *et al.* Seismic hydraulic fracture migration originated by successive deep magma pulses: The 2011–2013 seismic series associated to the volcanic activity of El Hierro Island. *J. Geophys. Res. Solid Earth* **120**, 7749–7770 (2015).

82. Maccaferri, F., Bonafede, M. & Rivalta, E. A quantitative study of the mechanisms governing dike propagation, dike arrest and sill formation. *J. Volcanol. Geotherm. Res.* **208**, 39–50 (2011).

83. Dixon, J. E., Stolper, E. M. & Holloway, J. R. An Experimental Study of Water and Carbon Dioxide Solubilities in Mid-Ocean Ridge Basaltic Liquids. Part I: Calibration and Solubility Models. *J. Petrol.* **36**, 1607–1631 (1995).

84. Vargas-Bracamontes, D. M. & Neuberg, J. W. Interaction between regional and magma-induced stresses and their impact on volcano-tectonic seismicity. *J. Volcanol. Geotherm. Res.* **243–244**, 91–96 (2012).

85. Rubin, A. M. & Gillard, D. Dike-induced earthquakes: Theoretical considerations. *J. Geophys. Res. Solid Earth* **103**, 10017–10030 (1998).

86. Harris, R. A. Large earthquakes and creeping faults. *Rev. Geophys.* **55**, 169–198 (2017).

87. Gillard, D., Rubin, A. M. & Okubo, P. Highly concentrated seismicity caused by deformation of Kilauea's deep magma system. *Nature* **384**, 343–346 (1996).

88. Phillips, T. B., Magee, C., Jackson, C. A.-L. & Bell, R. E. Determining the three-dimensional geometry of a dike swarm and its impact on later rift geometry using seismic reflection data. *Geology* **46**, 119–122 (2017).

89. McGarr, A. Maximum magnitude earthquakes induced by fluid injection. *J. Geophys. Res. Solid Earth* **119**, 1008–1019 (2014).

90. Bertiger, W. *et al.* GipsyX/RTGx, a new tool set for space geodetic operations and research. *Adv. Space Res.* **66**, 469–489 (2020).

91. Zumberge, J. F., Heflin, M. B., Jefferson, D. C., Watkins, M. M. & Webb, F. H. Precise point positioning for the efficient and robust analysis of GPS data from large networks. *J. Geophys. Res. Solid Earth* **102**, 5005–5017 (1997).

92. Bos, M. S., Araujo, I. & Bastos, B. L. Hector user manual version 1.1. (2013).

93. Fernandes, R. M. S. & Bos, M. S. Applied automatic offset detection using HECTOR within EPOS-IP. **2016**, G51A-1084 (2016).

94. González, P. J. Interferometric Synthetic Aperture Radar (InSAR). in *Remote Sensing for Characterization of Geohazards and Natural Resources* (eds. Chaussard, E., Jones, C., Chen, J. A. & Donnellan, A.) 53–73 (Springer International Publishing, Cham, 2024). doi:10.1007/978-3-031-59306-2_3.

95. Hogenson, K. *et al.* Hybrid Pluggable Processing Pipeline (HyP3): A cloud-native infrastructure for generic processing of SAR data. Zenodo https://doi.org/10.5281/ZENODO.4646138 (2024).

96. Instituto Português do Mar e da Atmosfera (IPMA). Portuguese National Seismic Network. International Federation of Digital Seismograph Networks https://doi.org/10.7914/SN/PM (2006).

97. Centro De Informação E Vigilância Sismovulcânica Dos Açores (CIVISA), U. O. A. CIVISA Seismo-Volcanic Monitoring Network-Azores Islands. Approximately 2 active stations GFZ Data Services https://doi.org/10.14470/PC311625 (2021).

98. Nuno Afonso Dias. Sao Jorge 2022. 500000 MB International Federation of Digital Seismograph Networks https://doi.org/10.7914/5C1J-6T82 (2025).

99. Ferreira, A. M. G., Ramalho, R. D. S. & Mitchell, N. Azores Network. 81000 MB International Federation of Digital Seismograph Networks https://doi.org/10.7914/FGP0-C809 (2026).

100. Ferreira, A. M. G., Mitchell, N., Ramalho, R. D. S., Hicks, S. & Tsekhmistrenko, M. São Jorge OBS Network. 115000 MB International Federation of Digital Seismograph Networks https://doi.org/10.7914/D5W4-V395 (2026).

101. Mousavi, S. M., Ellsworth, W. L., Zhu, W., Chuang, L. Y. & Beroza, G. C. Earthquake transformer—an attentive deep-learning model for simultaneous earthquake detection and phase picking. *Nat. Commun.* **11**, 3952 (2020).

102. Woollam, J. *et al.* SeisBench—A Toolbox for Machine Learning in Seismology. *Seismol. Res. Lett.* **93**, 1695–1709 (2022).

103. Münchmeyer, J. PyOcto: A high-throughput seismic phase associator. *Seismica* **3**, (2024).

104. Bornstein, T. *et al.* PickBlue: Seismic Phase Picking for Ocean Bottom Seismometers With Deep Learning. *Earth Space Sci.* **11**, e2023EA003332 (2024).
105. Winder, T. *et al. QuakeMigrate: A Modular, Open-Source Python Package for Automatic Earthquake Detection and Location*. https://essopenarchive.org/doi/full/10.1002/essoar.10505850.1 (2021) doi:10.1002/essoar.10505850.1.
106. Kissling, E., Ellsworth, W. L., Eberhart-Phillips, D. & Kradolfer, U. Initial reference models in local earthquake tomography. *J. Geophys. Res. Solid Earth* **99**, 19635–19646 (1994).
107. Hicks, S. P., Rietbrock, A., Ryder, I. M., Lee, C.-S. & Miller, M. Anatomy of a megathrust: The 2010 M8. 8 Maule, Chile earthquake rupture zone imaged using seismic tomography. *Earth Planet. Sci. Lett.* **405**, 142–155 (2014).
108. Bie, L. *et al.* Along-Arc Heterogeneity in Local Seismicity across the Lesser Antilles Subduction Zone from a Dense Ocean-Bottom Seismometer Network. *Seismol. Res. Lett.* **91**, 237–247 (2020).
109. Lomax, A. & Henry, P. Major California faults are smooth across multiple scales at seismogenic depth. *Seismica* **2**, (2023).
110. Lomax, A. & Savvaidis, A. High-Precision Earthquake Location Using Source-Specific Station Terms and Inter-Event Waveform Similarity. *J. Geophys. Res. Solid Earth* **127**, e2021JB023190 (2022).
111. Lomax, A., Tuvè, T., Giampiccolo, E. & Cocina, O. A new view of seismicity under Mt. Etna volcano, Italy, 2014-2023 from multi-scale high-precision earthquake relocations. *Ann. Geophys.* **67**, S437–S437 (2024).
112. Illsley-Kemp, F. *et al.* Local Earthquake Magnitude Scale and b-Value for the Danakil Region of Northern Afar. *Bull. Seismol. Soc. Am.* **107**, 521–531 (2017).
113. Satriano, C. SourceSpec – Earthquake source parameters from P- or S-wave displacement spectra. Zenodo https://doi.org/10.5281/zenodo.6954238 (2022).
114. Hicks, S. P. *et al.* Slab to back-arc to arc: Fluid and melt pathways through the mantle wedge beneath the Lesser Antilles. *Sci. Adv.* **9**, eadd2143 (2023).

115. Ross, Z. E., Ben-Zion, Y., White, M. C. & Vernon, F. L. Analysis of earthquake body wave spectra for potency and magnitude values: implications for magnitude scaling relations. *Geophys. J. Int.* **207**, 1158–1164 (2016).
116. Deichmann, N. Theoretical Basis for the Observed Break in ML/Mw Scaling between Small and Large Earthquakes. *Bull. Seismol. Soc. Am.* **107**, 505–520 (2017).
117. Staudenmaier, N., Tormann, T., Edwards, B., Deichmann, N. & Wiemer, S. Bilinearity in the Gutenberg-Richter Relation Based on ML for Magnitudes Above and Below 2, From Systematic Magnitude Assessments in Parkfield (California). *Geophys. Res. Lett.* **45**, 6887–6897 (2018).
118. Hicks, S. P. *et al.* A Shallow Earthquake Swarm Close to Hydrocarbon Activities: Discriminating between Natural and Induced Causes for the 2018–2019 Surrey, United Kingdom, Earthquake Sequence. *Seismol. Res. Lett.* **90**, 2095–2110 (2019).
119. Lanza, F., Thurber, C. H., Syracuse, E. M., Power, J. A. & Ghosh, A. Seismic tomography of compressional wave velocity and attenuation structure for Makushin Volcano, Alaska. *J. Volcanol. Geotherm. Res.* **393**, 106804 (2020).
120. Hudson, T. S., Kendall, J.-M., Pritchard, M. E., Blundy, J. D. & Gottsmann, J. H. From slab to surface: Earthquake evidence for fluid migration at Uturuncu volcano, Bolivia. *Earth Planet. Sci. Lett.* **577**, 117268 (2022).
121. Cao, A. & Gao, S. S. Temporal variation of seismic b-values beneath northeastern Japan island arc. *Geophys. Res. Lett.* **29**, 48-1-48–3 (2002).
122. Pugh, D. J. & White, R. S. MTfit: A Bayesian Approach to Seismic Moment Tensor Inversion. *Seismol. Res. Lett.* **89**, 1507–1513 (2018).
123. Cayol, V. & Cornet, F. H. 3D mixed boundary elements for elastostatic deformation field analysis. *Int. J. Rock Mech. Min. Sci.* **34**, 275–287 (1997).
124. Dumont, Q., Cayol, V. & Froger, J.-L. Mitigating bias in inversion of InSAR data resulting from radar viewing geometries. *Geophys. J. Int.* **227**, 483–495 (2021).
125. Sambridge, M. Geophysical inversion with a neighbourhood algorithm—I. Searching a parameter space. *Geophys. J. Int.* **138**, 479–494 (1999).

126. Fukushima, Y., Cayol, V. & Durand, P. Finding realistic dike models from interferometric synthetic aperture radar data: The February 2000 eruption at Piton de la Fournaise. *J. Geophys. Res. Solid Earth* **110**, 2004JB003268 (2005).
127. Yukutake, Y., Ueno, T. & Miyaoka, K. Determination of temporal changes in seismic velocity caused by volcanic activity in and around Hakone volcano, central Japan, using ambient seismic noise records. *Prog. Earth Planet. Sci.* **3**, 29 (2016).
128. De Plaen, R. S. M. *et al.* Temporal Changes of Seismic Velocity Caused by Volcanic Activity at Mt. Etna Revealed by the Autocorrelation of Ambient Seismic Noise. *Front. Earth Sci.* **6**, (2019).
129. Wu, S.-M. *et al.* Spatiotemporal Seismic Structure Variations Associated With the 2018 Kīlauea Eruption Based on Temporary Dense Geophone Arrays. *Geophys. Res. Lett.* **47**, e2019GL086668 (2020).
130. Schimmel, M., Stutzmann, E. & Gallart, J. Using instantaneous phase coherence for signal extraction from ambient noise data at a local to a global scale. *Geophys. J. Int.* **184**, 494–506 (2011).
131. Schimmel, M., Stutzmann, E. & Ventosa, S. Low-Frequency Ambient Noise Autocorrelations: Waveforms and Normal Modes. *Seismol. Res. Lett.* **89**, 1488–1496 (2018).
132. Sánchez-Pastor, P., Obermann, A. & Schimmel, M. Detecting and Locating Precursory Signals During the 2011 El Hierro, Canary Islands, Submarine Eruption. *Geophys. Res. Lett.* **45**, 10,288-10,297 (2018).
133. Minshull, T. A., Sinha, M. C. & Peirce, C. Multi-disciplinary, sub-seabed geophysical imaging-a new pool of 28 seafloor instruments in use by the United Kingdom Ocean Bottom Instrument Consortium. *Sea Technol.* **46**, (2005).
134. Hicks, S. Supplementary data for 'Leaky faults modulated magma ascent and adjacent seismicity during the 2022 São Jorge Island (Azores) seismic-volcanic unrest' by Hicks, Gonzalez, et al. Zenodo https://doi.org/10.5281/zenodo.14421663 (2024).
135. EMODnet Bathymetry Consortium. EMODnet Digital Bathymetry (DTM 2022). EMODnet Bathymetry Consortium

https://doi.org/10.12770/FF3AFF8A-CFF1-44A3-A2C8-1910BF109F85 (2022).